Lithos 396–397 (2021) 106224

Contents lists available at ScienceDirect

Lithos

journal homepage: www.elsevier.com/locate/lithos

Research Article

Experimental investigation of the composition of incipient melts in upper mantle peridotites in the presence of CO_2 and H_2O

Zsanett Pintér [a,b,c,*], Stephen F. Foley [a,b], Gregory M. Yaxley [b], Anja Rosenthal [b,d], Robert P. Rapp [b,e], Anthony W. Lanati [a,f], Tracy Rushmer [a]

[a] Department of Earth and Environmental Sciences and ARC Centre of Excellence for Core to Crust Fluid Systems (CCFS), Macquarie University, North Ryde, NSW 2109, Australia
[b] Research School of Earth Sciences, Australian National University, Canberra, ACT 2601, Australia
[c] School of Earth & Atmosphere and Environment, Monash University, Clayton, VIC 3800, Australia
[d] ESRF - The European Synchrotron, 71 Avenue des Martyrs, 38043 Grenoble, France
[e] Hawaii Institute of Geophysics and Planetology, University of Hawaii at Manoa, Honolulu 96822, HI, United States of America
[f] Institut für Mineralogie, Westfälische Willhelms-Universität Münster, Corrensstraße 24, D-48149 Münster, Germany

ARTICLE INFO

Article history:
Received 16 January 2021
Received in revised form 4 May 2021
Accepted 7 May 2021
Available online 14 May 2021

Keywords:
Experimental petrology
Peridotitic upper mantle melting
Volatiles (CO_2-H_2O)
Incipient melting
Ultramafic lamprophyre
Carbonatite

ABSTRACT

The compositions of mantle-derived magmas indicate a substantial variety in the abundances of volatiles in the upper mantle. CO_2 and H_2O depress the melting point of mantle peridotites considerably, delineating a pressure-temperature region of incipient melting where small degrees of melt exist over a large temperature range (~300 °C) before major melting begins. However, the chemical characterization of these melts in high-pressure experiments is challenging at low melt fractions (melt pockets may occupy volumes of only 10–50 μm^3) because of analytical uncertainties related to the ubiquitous formation of metastable phases during quenching.

This systematic partial melting study presents carefully determined compositions of incipient melts of a range of peridotites in the presence of $CO_2 + H_2O$ mixtures at 2.5 to 7 GPa. Four different fertile and depleted peridotites were used: Hawaiian pyrolite, K_2O-enriched pyrolite, MORB pyrolite and depleted lherzolite. To arrive at accurate melt compositions, we introduce the *melt tomography* method that integrates multiple area scans of melt pockets polished to several depths. Results confirm that incipient and low degree melts progress abruptly (within 25 °C) from carbonatitic towards melilititic-nephelinitic compositions at 2.5 GPa, whereas they progress gradually from carbonate-rich to carbonated silicate (aillikitic) compositions at 4–5 GPa. Melt compositions at near-solidus conditions are mainly controlled by the breakdown of carbonate, and hydrous phases such as pargasite and phlogopite, and become less siliceous and slightly more magnesian with increasing pressure at given melt fractions. Melts exhibit strong increases in SiO_2 (2.75 to 44 wt%) with increasing temperature, whereas TiO_2, Na_2O and K_2O decrease. The generally strongly potassic ($K_2O \leq 6.63$ wt%) and sodic ($Na_2O \leq 3.06$ wt%) character of the volatile-rich, incipient and low-degree melts indicate that these would act as reactive metasomatic agents that may transport large amounts of energy and induce chemical changes in large volumes of the upper mantle.

1. Introduction

Volatile components (H_2O, CO_2, $CO_2 + H_2O$, $CH_4 + H_2O$) depress the melting point of peridotites considerably (e. g. Green, 2015; and references therein), defining an incipient melting regime, which extends over a large temperature interval (~300 °C) in the upper mantle. In this incipient melting regime, only low degree, volatile-rich melts are stable before major melting of four-phase peridotite begins (Green, 2015). These incipient melts are probably instrumental in transporting heat, volatiles and alkalis through the upper mantle, causing metasomatic overprints and possibly explaining the low velocity signals in P-wave studies (Green, 1976). However, incipient melts in the upper mantle probably have no direct compositional analogues in volcanism at the Earth's surface, although they are probably most closely related to carbonatites, kimberlites, kamafugites and ultramafic lamprophyres (Foley and Pintér, 2018). Indirect indications of the compositions of these melts are available in modally and cryptically metasomatized upper mantle xenolith suites sampled by various mantle-derived magmas (O'Reilly and Griffin, 2013; Yaxley et al., 1991).

The study of incipient melts in high pressure experiments is challenging, because low degree melts in small pools make the poorly-quenched melts difficult to characterise (Dasgupta and Hirschmann, 2006; Green et al., 2014; Walter, 1998). Previous experimental studies have attempted to pinpoint equilibrium melt compositions with

---

* Corresponding author at: School of Earth & Atmosphere and Environment, Monash University, Clayton, VIC 3800, Australia.
E-mail address: zsanett.pinter@monash.edu (Z. Pintér).

https://doi.org/10.1016/j.lithos.2021.106224

different experimental setups, including partial melting experiments with melt traps to form larger, analysable melt pockets (Hirose & Kushiro, 1993; Dasgupta and Hirschmann, 2006; Tumiati et al., 2013; Green et al., 2010, 2014; Dvir and Kessel, 2017; Sorbadere et al., 2018); sandwich experiments (Wallace and Green, 1988) and iterative sandwich experiments that use partition coefficients to access equilibrium compositions (Dasgupta and Hirschmann, 2007; Falloon et al., 2008; Novella and Frost, 2014). Here, we introduce a new technique with which rigorous melt compositions are reconstructed from heterogeneously quenched melt pools at several levels through the section of the experimental samples. It is crucial to correctly characterise melt compositions in order to understand incipient/partial melting of various volatile-bearing peridotite compositions, and to reconstruct the metasomatic effects they may have on different mantle regions.

Previous experiments focused on natural and simplified mantle peridotite compositions, mostly under oxidizing conditions in the presence of H_2O (Green et al., 2010, 2014) or CO_2 (Eggler, 1978; Dasgupta et al., 2007, 2013; Dasgupta and Hirschmann, 2006). However, few experimental studies have examined peridotites containing both H_2O and CO_2 (Wallace and Green, 1988); Brey et al., 2009; Foley et al., 2009; Green et al., 2010, 2014; Litasov et al., 2011; Tumiati et al., 2013; Dvir and Kessel, 2017) and even fewer experimental studies have investigated melting and phase relations of peridotites with C-O-H volatile mixtures under reducing conditions (Foley and Pintér, 2018; Litasov et al., 2014; Taylor and Green, 1988 and references therein).

In this paper, we present an extensive experimental investigation of partial melts of four different model peridotite compositions in the presence of $CO_2 + H_2O$ to explore the range of incipient melt compositions, supplementing those of Wallace and Green (1988) and Foley et al. (2009), which focused on enriched pyrolite along the oxidized solidus. In this study, the four starting compositions represent a large palette of chemical and volatile compositions across peridotites from modally metasomatized, carbonated K-enriched lherzolite to volatile-saturated, modally unmetasomatized fertile and refractory peridotite.

2. Experimental strategy – choice of starting compositions

The main aim of this experimental investigation is to explore the effect of the variation in peridotite composition in source regions on the compositions of volatile-bearing mantle-derived melts. This study focuses on the compositions of near-solidus melts over a relatively large compositional range from 2.5 to 7 GPa. Four peridotites were chosen as starting compositions (Table 1): (1) HPK with 2.88 wt% CO_2 and 0.58 wt% H_2O is based on Hawaiian pyrolite (HP) with added K_2O to investigate the role of phlogopite in low degree melting (Foley et al., 2009). The CO_2 and H_2O contents added here are slightly less than in the study of Foley et al. (2009), who added 3.2 wt% CO_2 and 0.63 wt% H_2O to HPK. (2) HP is a fertile Hawaiian pyrolite. It is an estimate of the composition of the mantle source for Hawaiian olivine tholeiites, and which has been used in previous studies (Foley et al., 2009; Wallace and Green, 1988). Similar amounts of CO_2 and H_2O as for HPK were included. HP and HPK represent enriched, modally metasomatized mantle compositions. (3) HZ1 is a model lherzolite with composition close to MORB pyrolite, devised as an estimate for mid-ocean ridge basalt (MORB) source regions (Hart & Zindler, 1986; Green et al., 2010, 2014), and here includes 0.95 wt% CO_2 and 0.48 wt% H_2O. (4) The refractory Tinaquillo lherzolite (TQ), to which 0.3 wt% CO_2 and 0.3 wt% H_2O were added, is a model mantle composition more depleted in Na_2O, TiO_2 and K_2O (Green, 2015). The volatile contents in HPK, HP, HZ1 and TQ experiments were chosen to lie above the volatile storage capacity of nominally volatile-free lherzolitic assemblies at the targeted upper mantle pressure-temperature conditions. To prevent leaching of components such as Al_2O_3, Na_2O and K_2O in the presence of extensive excess of volatiles, in particular H_2O (Green et al., 2014), a lower amount of volatiles was included for HZ1 and TQ because of their more depleted character relative to HPK and HP.

Table 1
Compositions of the starting mixtures for the high-pressure experiments. HPK = K-enriched Hawaiian pyrolite, HP = Hawaiian pyrolite, HZ1 = mid-ocean ridge pyrolite, TQ = depleted lherzolite.

	K-enriched Hawaiian Pyrolite (HPK)	Hawaiian Pyrolite (HP)	Fertile lherzolite (HZ1)	Tinaquillo lherzolite (TQ)
SiO_2	42.86	43.45	43.93	44.53
TiO_2	0.67	0.68	0.17	0.08
Cr_2O_3	0.41	0.41	0.38	0.45
Al_2O_3	3.36	3.40	3.88	3.19
FeO	8.03	8.14	7.22	7.59
MgO	35.56	36.05	36.10	39.66
CaO	2.92	2.96	3.07	2.96
MnO	0.09	0.10	0.10	0.00
NiO	0.19	0.19	0.00	0.26
Na_2O	0.54	0.55	0.31	0.18
K_2O	1.42	0.12	0.03	0.02
H_2O	0.58	0.58	0.48	0.30
CO_2	2.88	2.88	0.95	0.30
Trace element mix	0.48	0.48	0.48	0.49
Ir	0	0	2.91	0
Total	100	100	100	100

HPK: after Foley et al., 2009; HP after Wallace & Green, 1989.
H2O added as as Mg(OH)2 in all four mixes, CO2 added as CaCO3 in all four mixes.
Trace element mix: 1000 ppm wt% Nb, 700 ppm wt% La and 500 ppm wt% Y, Zr, Ho, Lu, Hf, Ta.

3. Experimental setup and analytical methods

3.1. Starting compositions

One gram batches of each peridotite starting composition (HPK, HP, HZ1, TQ; Table 1), were prepared by blending high purity synthetic oxide powders (MgO, SiO_2, TiO_2, Al_2O_3, MnO, Cr_2O_3) and carbonates ($CaCO_3$, Na_2CO_3, K_2CO_3) together under acetone and then firing the resultant, fine-grained, homogenous mix at 1000 °C for 12 h. Additionally, NiO was added to HPK, HP and TQ. A small amount of Ir powder was added to the HZ1 composition as a redox sensor, for which results are reported in Supplementary Table 3 and Supplementary S1.4. Iron was then added as synthetic fayalite (Fe_2SiO_4), H_2O as $Mg(OH)_2$ and CO_2 as $CaCO_3$. All four synthetic mixes were doped with a trace element mixture containing eight elements at concentrations of 500–1000 ppm (Y, Zr, Nb, La, Ho, Lu, Hf, Ta; Table 1). These were chosen to monitor behaviour seen in a previous study (Foley et al., 2009) where Ho, La and Lu showed enrichment, while strong Nb and Ta, and slight Hf and Y depletion patterns were observed for melts with carbonatitic rather than carbonated silicate melt affinity.

3.2. Experimental methods

We used established experimental procedures, similar to Foley et al. (2009). Starting powders for piston cylinder experiments (one each of HPK, HP, HZ1, TQ) were loaded into a 0.45 mm long graphite capsule (1.9 mm OD and 1 mm ID) with graphite lid (2.3 mm OD, 1.9 mm ID) which was then dried in a vacuum furnace overnight. These graphite inner capsules were then placed in Au outer capsules (2.3 mm OD, 1.9 mm ID). Two capsules (with graphite inner and gold outer capsule), containing either HPK and HP, or HZ1 and TQ, were included in each experiment, ensuring the temperatures and pressures are identical for experiments with these two sets of mixes.

Experiments were conducted in end-loaded Boyd-England half-inch (1.27 cm) piston cylinder apparatuses (200 T and 500 T presses) at the Research School of Earth Sciences (RSES), Australian National University

(ANU) at pressures from 2.5 to 5.0 GPa and temperatures from 990 to 1210 °C for 48–96 h (Fig. 1, Table 2). NaCl cells with pyrex and MgO inserts were used as pressure media, heaters were straight graphite cylinders, and temperatures were monitored with B-type thermocouples (with no correction for the effect of pressure on the thermocouple emf) and controlled to within ±2 °C of the set point using a Eurotherm controller. Experiments were conducted with the hot piston-in technique.

For experiments conducted with the multi anvil device at RSES, ANU, four gold capsules with 1 mm OD, each filled with one of the four different starting compositions (HPK, HP, HZ1, TQ) were cemented in a cylindrical MgO holder (Fig. 1). The standard 14/8 COMPRES Cr-doped MgO experimental octahedron assembly consists of semi-sintered ZrO_2 insulation sleeves and internal spacers of MgO (Leinenweber et al., 2012). The cell assembly consists of MgO sleeves above and below the MgO cup in the geometric centre of the graphite furnace (run number MA1161, Fig. 1) or *Re*-foil heater (run number MA1163). Temperature was controlled to ±1 °C using D-type thermocouples (W_3Re_{97}-$W_{25}Re_{75}$). Experiments at 7 GPa and 1170–1210 °C were performed using a 1200-ton uniaxial press with a Kawai-type, split-sphere 6/8 multi anvil device at RSES, ANU for 12 h (Fig. 1, Table 2), using established experimental procedures and calibration.

3.3. Approach to equilibrium

A close approach to equilibrium in the experiments was optimized by ensuring homogeneity of the starting materials and accurate assembly preparation, by choosing long experiment durations under stable pressure and temperature conditions, and by quenching rapidly. Major and minor element compositions of minerals are homogeneous apart from very minor zoning of Al_2O_3, MgO, and CaO in garnets (Supplementary S1.3 and Table S2), which is a common phenomenon in high-pressure experiments (Dasgupta and Hirschmann, 2007; Spandler et al., 2008).

3.4. Preparation of run products for phase characterization and analysis

After quenching the experiments, capsules were closely examined and weighed. Any capsules that showed signs of cracks in the gold walls or weight loss were discarded as having suffered volatile loss. Gold capsules are documented to seal volatiles with the least loss inside the sample chamber (Demouchy and Bolfan-Casanova, 2016; Demouchy and Mackwell, 2006; Green, 1976). Capsules were sectioned longitudinally, embedded in epoxy mounts, and ground and polished under petroleum ether, avoiding contact with water to eliminate the possibility of dissolution of alkali carbonates (Foley et al., 2009; Wallace and Green, 1988). Once the capsules were breached, epoxy was drawn multiple times (4–7 times each capsule) into the charge to minimize the loss of minerals and quenched melts during polishing.

3.5. Determination of accurate melt compositions using the melt tomography technique

Volatile-rich partial melts of peridotite never quench to homogeneous glasses but form complex mats of quenched crystals of metastable minerals up to several μm in size, leading to heterogeneity in the quenched melts (Fig. 2., e.g. Green, 1973, 1976; Dasgupta and Hirschmann, 2006; Foley et al., 2009; Green et al., 2014; this study). We developed the *melt tomography* technique to determine accurate melt compositions and investigate the heterogeneity and/or homogeneity of quenched volatile-rich low-silica melts.

For piston-cylinder experiments, scanning electron microscopy (SEM) and microprobe area analyses of exposed melt pools were conducted, after which sections were repolished to expose deeper levels of the same melt pools. The reported melt compositions are the integrated analyses of the same melt pools on several (2–5) polished surfaces, successively exposed by progressively removing ~5–15 μm of material, re-polishing, and re-analysing the new surface. Averaged melt compositions were determined by imaging and integrating area analyses from ~25 to ~1500 μm^2 with a defocused microprobe beam and calibrated areal SEM measurements (Figs. 3 & 4). This method allows averaging of the heterogeneously quenched melt pool composition (Figs. 3 & 4). However, multi-anvil experimental capsules could be exposed and analysed only once due to the smaller capsule size (~0.4 mm ID sample size) and smaller partial melt volume (~15–35 μm^3).

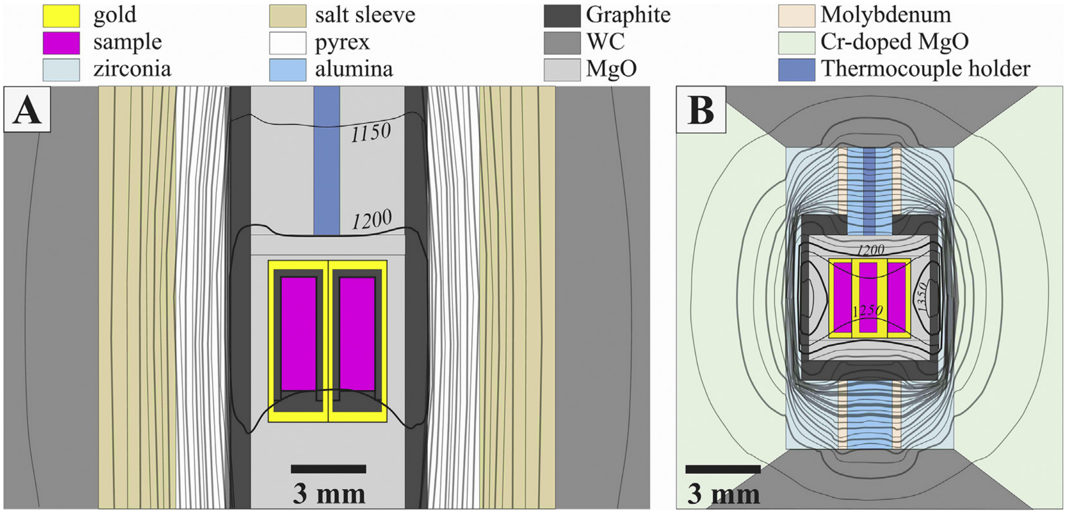

Fig. 1. Cross sections through the experimental assemblies used in this study. (A) Thermal contours calculated for the ½" piston cylinder buffer assembly with central temperature of 1200 °C (thick contour intervals are 100 °C; thinner lines 50 °C intervals). The two-capsule configuration is shown with gold outer and straight graphite inner capsules, oriented with graphite lids at the bottom. (B) Thermal contours generated using the CellAssembly program (by Hernlund et al., 2006) for the 14/8 COMPRES multi anvil assembly (G2) in a four-capsule configuration with central temperature of 1250 °C and 1210 °C at the top of the capsule. Contour intervals: thick lines 100 °C, thin lines 50 °C). Cell assembly setup after Leinenweber et al. (2012). (For interpretation of the references to colour in this figure legend, the reader is referred to the web version of this article.)

Table 2
Experimental conditions and run results of experiments using HPK, HP, HZ1 and TQ starting materials.

Experiment	P (GPa)	T (°C)	Duration (h)	Capsule type	Phase proportions [%]	Maximum C content of residua [ppm]	Maximum H_2O content of residua [ppm]
F001-HPK	2.5	990	96	Au + gr	ol [47.3], opx [21.1], cpx [6.3], sp. [0.1], phl [16.5], amph [1.9], melt [6.9]	1.1	7104
E002-HPK	2.5	1090	72	Au + gr	ol [41.4], opx [29.9], cpx [5.3], phl [14.2], amph [1.2], melt [8.0]	1.2	6086
F015-HPK	2.5	1130	48	Au + gr	ol [50.3], opx [23.6] amph [5.0], melt [21.1]	0.9	921
F017-HPK	*4*	*1020*	96	Au + gr	ol [47.4], opx [19.9], cpx [5.9], ga [5.8], phl [13.6], fluid+melt quench [7.3]	1.1	5663
F003-HPK	4	1040	96	Au + gr	ol [45.7], opx [28.0], cpx [6.1], ga [6.5], phl [6.8], melt [6.9]	1.3	2969
F004-HPK	4	1090	96	Au + gr	ol [46.6], opx [26.5], cpx [4.2], ga [8.7], phl [4.1], melt [9.9]	1.2	1863
F013-HPK	4	1170	95	Au + gr	ol [47.9], opx [23.7], cpx [4.1], ga [7.2], melt [17.2]	1.2	221
HP009-HPK	5	1090	72	Au + gr	ol [38.1], opx [34.3], cpx [2.0], ga [6.6], phl [4.3], carb min [3.1], melt [11.7]	1.4 [wt%] *	2222
HP012-HPK	5	1170	72	Au + gr	ol [46.2], opx [36.7], cpx [1.2], ga [11.8], melt [14.5], carb intersticial melt [0.1]	2.1	514
HP014-HPK	5	1210	48	Au + gr	ol [42.6], opx [28.4], cpx [3.4], ga [4.5], melt [21.1]	1.6	395
MA1163-HPK	7	1210	12	Au	ol [~34], opx [~39], ga [~13], melt[~14]	2.5	431
F001-HP	2.5	990	96	Au + gr	ol [49.6], opx [26.9], cpx [5.9], ga [3.8], amph [3.1], fluid+melt quench [10.8]	1.3	710
E002-HP	2.5	1090	72	Au + gr	ol [51.4], opx [20.9], cpx [0.3], sp. [0.3], amph [12.4], phl [0.9], melt [13.8]	0.9	2387
F015-HP	2.5	1130	48	Au + gr	ol [52.5], opx [19.8], melt [27.7]	0.9	163
F003-HP	4	1040	96	Au + gr	ol [43.7], opx [31.9], cpx [3.1], ga [11.9], phl [1.3], melt [8.1]	1.4	758
F004-HP	4	1090	96	Au + gr	ol [41.1], opx [33.9], cpx [1.8], ga [12.6], phl [1.4], melt [9.2]	1.4	788
F013-HP	4	1170	95	Au + gr	ol [51.7], opx [19.5], cpx [4.5], ga [7.5], melt [16.8]	1.1	219
HP009-HP	5	1090	72	Au + gr	ol [50.5], opx [18.2], cpx [8.3], ga [10.7], fluid quench [12.4]	2.0	489
HP014-HP	5	1210	48	Au + gr	ol [43.6], opx [29.5], cpx [0.5], ga [11.1], melt [15.3]	1.9	441
MA1163-HP	7	1210	12	Au	ol [~38], opx [~34], ga [~18], melt [~10]	2.7	465
F005-HZ1	2.5	990	95	Au + gr	ol [49.1], opx [19.3], cpx [14.9], sp. [2.6], amph [6.7], melt [7.4]	1.3	1306
E006-HZ1	3.5	1090	96	Au + gr	ol [51.3], opx [21.5], ga [5.2], melt [22.1]	1.0	176
HP007-HZ1	5	*1140*	70	Au + gr	ol [47.1], opx [26.7], cpx [7.2], ga [16.1], melt [3.0]	2.2	538
HP010-HZ1	5	1170	72	Au + gr	ol [50.5], opx [29.4], ga [13.9], melt [6.3]	2.0	473
MA1161-HZ1	7	1170	12	Au	ol [~35], opx [~41], ga [~19], melt [~4]	2.8	508
MA1163-HZ1	7	1210	12	Au	ol [~38], opx [~30], cpx [~7], ga [~18], melt [~7]	2.9	526
F005-TQ	2.5	990	95	Au + gr	ol [55.8], opx [24.9], ga [11.0], melt [8.2]	1.2	207
HP010-TQ	5	1170	72	Au + gr	ol [49.0], opx [34.6], ga [13.2], melt [3.3]	2.1	229
MA1161-TQ	7	1170	12	Au	ol [~49], opx [~25], ga [~15], melt [~11]	2.9	440
MA1163-TQ	7	1210	12	Au	ol [~43], opx [~39], ga [~13], melt [~5]	2.9	505

ol= olivine, opx= orthopyroxene, cpx= clinopyroxene, ga= garnet, sp= spinel, amph= amphibole, phl= phlogopite, carb min = carbonate, carb = carbonatitic melt.
Au + gr: graphite-lined Au-capsules.
All piston-cylinder experiments used NaCl + straight graphite furnaces + pyrex + MgO-Al2O3, except run F001, F003 and F017 used mullite instead of Al2O3.
All multi-anvil experiments used 14/8 COMPRESS assembly and a graphite heater (MA1161) or a Re-foil heater (MA1163).
*=estimation is in wt% CO2, reads as 1.4 wt% CO2. It is based on the determined dolomitic carbonate of this run, namely Ca86Mg14(CO3)2 (see STable 2).

3.6. Calculation of modal proportions

Modal proportions of all experiments were calculated by matching the average major and minor element compositions of the phases to the bulk starting compositions (HPK, HP, HZ1, TQ) by sum of least squares mass balance regression using StatPlus®. We followed the approach of Green et al. (2014) in determining modal proportions of hydrous phases (amphibole, phlogopite) and melt. Where it was possible to do so, modal proportion estimates based on textural observation were attempted for comparison with calculations made by the Green et al. (2014) method, revealing good agreement, to within 1.0% (absolute).

3.7. Analytical techniques

Quantitative major and minor element analyses of the melts were obtained using a JEOL 8530F Plus field emission (FE) electron microprobe operating at 10 kV accelerating and 3 nA beam current, and additionally by performing area scans (usually 5–10 μm^3, seldom up to 30 μm^3) using a quantitatively calibrated energy dispersive spectrometry (EDS) detector of a FE-SEM (Hitachi 4300 SE/N Schottky Field Emission) operated at 6 kV and 3 nA. Both instruments are housed at the Centre of Advanced Microscopy (CAM), ANU.

The loss of K, Na, and Ca during the interaction of the beam with sensitive melt pools was considerably less extensive than in previous analytical setups due to the low kV and beam current and the broad area analysis of the FE-SEM. The accuracy of the EDS/SEM method at ANU has previously been demonstrated (Green et al., 2014; Hermann et al., 2005; Spandler et al., 2008, 2010).

Crystalline phases were quantitatively analysed with a focused (<1 μm diameter) 10 nA beam by wavelength dispersive spectrometry (WDS) with an acceleration voltage of 15 kV, using the electron microprobe facilities (Cameca SX100 and JEOL 8530F Plus) at RSES and CAM, respectively. Counting times were 20 s on the peak position and 10s on background.

3.8. Estimation of the volatile contents of melts

The low totals of analyses of quenched liquids indicate substantial volatile contents (Table 3). Hydrous carbonatitic and silica-undersaturated silicate melts never quench to homogeneous glasses, but rather to mats of quenched minerals (Figs. 2, 3 & 4), hampering the direct analysis of volatiles. Therefore, the volatile contents of incipient melts in experiments were estimated based on a parameterization of melt compositions using major and minor elements in combination with the known mineralogy of hydrous carbonated peridotites. Details are provided in the Supplementary Materials (S1.6).

At pressures greater than ~2 GPa at near-solidus temperatures, CO_2 vapour interacts with silicate phases to form dolomite or magnesite at sub-solidus conditions (Dasgupta and Hirschmann, 2006; Green, 2015 and references therein). Applying the approach of Ghosh et al. (2014), CO_2 contents of the experimental melts were estimated based on their measured CaO, MgO and their ratios (Ca/(Ca + Mg)).

The H_2O contents of melts were estimated from bulk initial H_2O and K_2O contents and the H_2O contents of the hydrous phases amphibole and phlogopite. At low pressures (2.5 GPa) K is supplied by the breakdown of both phlogopite and amphibole, while at higher pressures (4–5 GPa) K is supplied mainly by phlogopite with a very minor

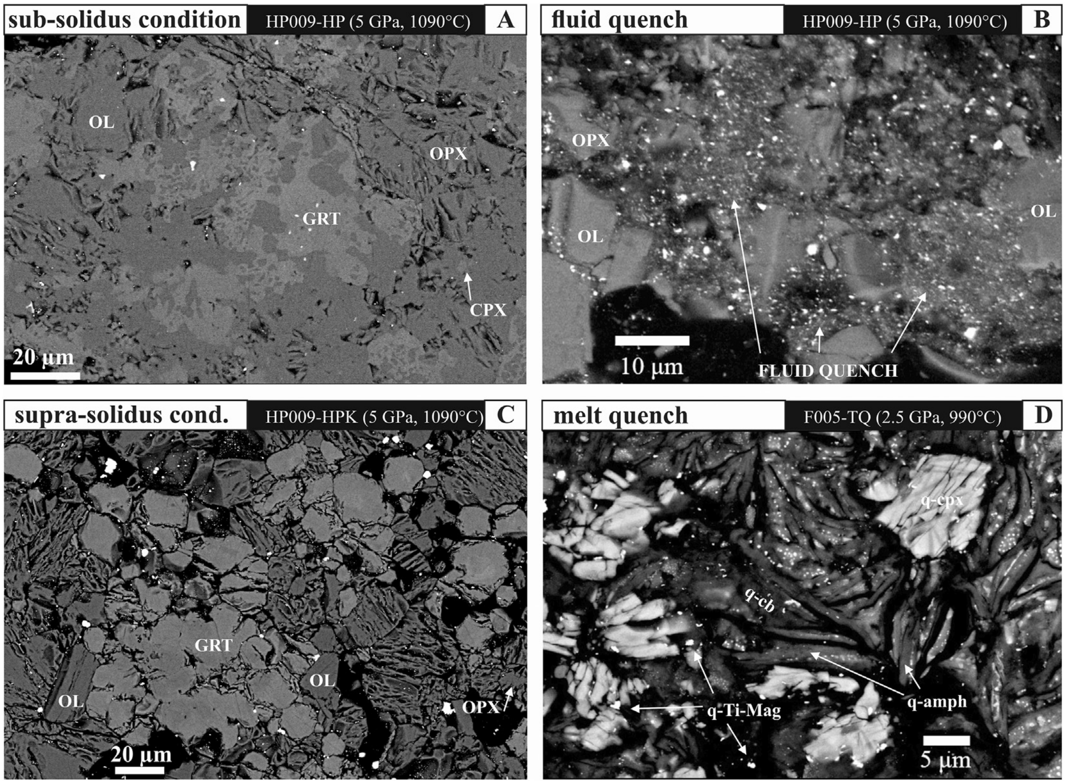

Fig. 2. Back-scattered images of textures of experimental products from run (HP009) at 5 GPa, 1090 °C (A-C). Mineral assemblages (A) under vapour-saturated sub-solidus conditions (HP009-HP) and (C) at vapour-deficient supra-solidus conditions (HP009-HPK). Textural difference between melt and fluid quench shown in B-D; B) Back-scattered electron (BSE) image of fluid quench texture showing fragmented films of glass surrounded by olivine grains (experiment HP009-HP). D) quenched melt in an intersertal texture in residual harzburgite F005-TQ (2.5 GPa, 990 °C) in high-resolution BSE image showing quenched intergrowths of amphibole (q-amp), clinopyroxene (q-cpx), carbonate (q-cb), titanomagnetite (q-Ti-Mag). Ol: olivine, opx: orthopyroxene, cpx: clinopyroxene, grt: garnet.

contribution from clinopyroxene in the enriched HPK and HP peridotite compositions.

4. Results

Phase assemblages and proportions determined by mass-balance (see 3.6 for more details) are presented in Table 2, Supplementary S1.3 section, Supplementary Table 2 and Fig. S2. The degree of melting is low to moderate in all experiments (< 28%, Tables 2, 3). Table 3 and Supplementary Table 1 summarize the major and minor element compositions (wt%) of the quenched melts and solid phases, respectively, for all experiments.

4.1. Textures of run products and quenched melts

Experimental run products consist of olivine, orthopyroxene ±spinel (2.5 GPa), ±garnet (3.5–7 GPa), ±clinopyroxene (2.5–7 GPa), ±ilmenite (2.5 GPa), ±pargasite (2.5 GPa), ±phlogopite (2.5–5 GPa) and ± carbonate (5 GPa) in equilibrium with heterogeneously quenched melt (Table 2, S2, Fig. 9, Fig. S2). The sub-solidus run (HP009-HP)

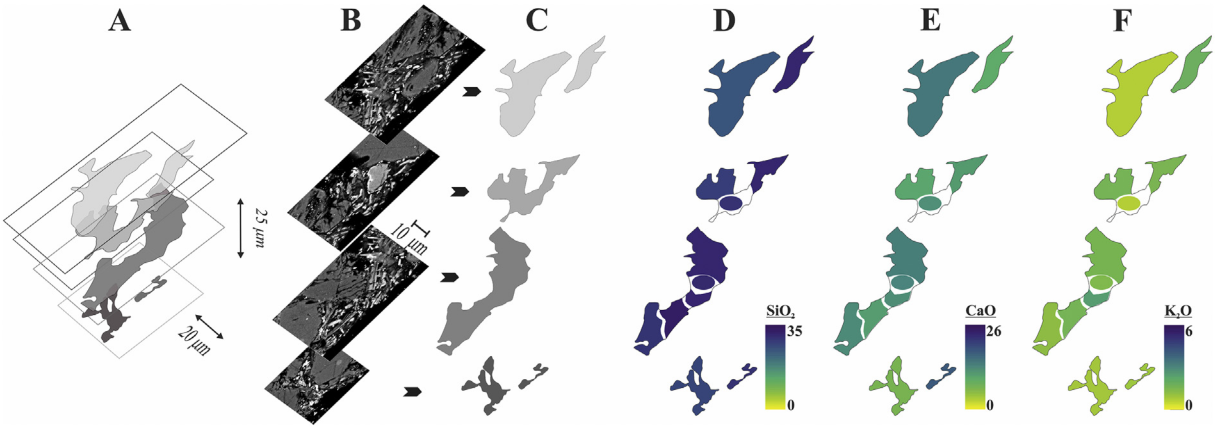

Fig. 3. Melt tomography of homogeneously quenched melt pool from F001-HP (2.5 GPa, 990 °C) (A). (B) BSE images of each exposed slice and (C) shape of the melt pool in each slice. Chemical composition of the melt pool shown as (D) SiO_2, (E) CaO and (F) K_2O contents of each melt slice. Defocused microprobe measurements are coloured ovals, while area analyses obtained with FE-SEM are represented by shaded regions.

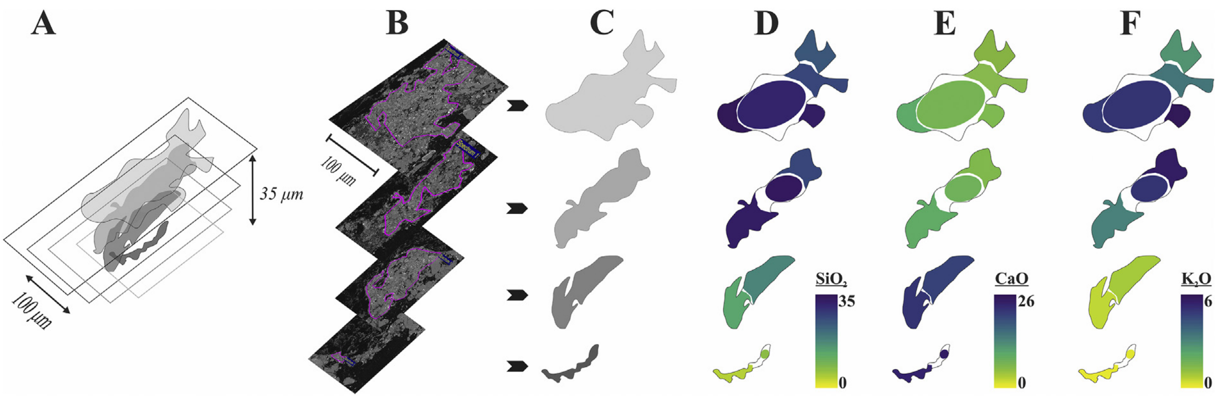

Fig. 4. Melt tomography of heterogeneously quenched melt pool from F004-HPK (4 GPa, 1090 °C) (A). (B) BSE images of each exposed slice and (B) shape of the melt pool in each slice. Chemical composition of the melt pool; (D) SiO_2, (E) CaO and (F) K_2O contents of each melt slice. Defocused microprobe measurements are coloured ovals, while area analyses obtained with FE-SEM are represented by shaded regions. Heterogeneously quenched carbonatitic mats are present in the bottom of the melt pool (with low SiO_2 and high CaO contents, D-E), whereas quenched phlogopite mats are concentrated at the top and edges of the melt pool (F).

contains fine-grained subhedral crystals of garnet (<10 µm), and olivine and clinopyroxene often appear as small inclusions in garnet (Fig. 2A). The supra-solidus run (HP009-HPK) contains larger euhedral and subhedral garnet (>20 µm) (Fig. 2C). Meanwhile at near- and supra-solidus conditions, euhedral and subhedral olivine, and orthopyroxene ± (spinel/garnet, clinopyroxene, phlogopite, amphibole, carbonate) are residual phases (Table 2). Grain sizes increase (~5–70 µm) with increasing temperature (Fig. 2C).

At 2.5 GPa, amphibole and phlogopite remain residual phases in HPK and HP at near-solidus conditions (Table 2; S2, Fig. 9, Fig. S2), while amphibole disappears towards higher pressures. Phlogopite persists up to 4 GPa in near-solidus HP runs and to 5 GPa in HPK. In HZ1, at 2.5 GPa, amphibole remains the only stable hydrous phase coexisting with a low degree of partial melt at 990 °C, but is absent at higher pressures (3.5–7 GPa). At 5 GPa, clinopyroxene melts out first in the four-phase lherzolitic assemblage between 1140 and 1170 °C. In TQ, both hydrous phases amphibole and phlogopite as well as clinopyroxene are always absent as residual phases, leaving a residual garnet-bearing harzburgite in association with a melt fraction at all conditions studied.

Quenched vapours and volatile-rich melts were distinguished following criteria described by Green (1973, 1976) and Green et al. (Green et al., 2010, Green et al., 2014; Fig. 2). Fluid quenches to thin films, fragmented filaments in void spaces, and coats neighbouring olivine and orthopyroxene crystals. This is evident in sub-solidus run HP009-HP (5 GPa, 1090 °C), which contains a quenched vapour phase (Fig. 2B, Tables 2, 3). Interestingly, amphibole- and phlogopite-bearing lherzolite F001-HP (2.5 GPa, 990 °C) and F017-HPK (4 GPa, 1020 °C) each contain a quenched vapour phase in close association with a quenched melt.

In contrast, melts show strong quenching effects, usually with crystal overgrowths (~0.1–7 µm), films or spheres of modified glass and even pores (Fig. 2D). Quenched melt pools in experimental run products consist mainly of mats of metastable silicate, carbonate and oxide crystals, each up to several µm in size (Fig. 2D). They usually contain quenched glass, non-stochiometric phases including phlogopite (in HPK and HP experiments), clinopyroxene, titanomagnetite, amphibole, ilmenite and dolomitic carbonate.

Melts in piston cylinder experiments were often ponded at the top margins of the graphite capsule and found interstitially between olivine and garnet grains. All but two (MA1163-HPK, MA1161-TQ) multi anvil experiments at 7 GPa show an ‘hourglass shaped’ melt distribution around the centre of capsules. The two capsules that do not have probably moved during the experiment and correspond to hotter conditions than shown by the thermocouple.

4.2. Results of tomography of melts

Generally, the compositions of exposed melt pools from each piston cylinder experiment show good agreement between different polished surfaces (e.g. Fig. 3), although some small melt pools show a stronger degree of heterogeneity, expressed as a concentration of quenched carbonates at the edges and bottom (e.g. Fig. 4) in F004-HPK (4GPa, 1090 °C) and HP010-TQ (5GPa, 1170 °C). Fig. 5 shows the distribution of K_2O in all measured melt pools: this highlights the variety of quenching effects in the melt pools and underscores the need for careful integration and reconstruction of the entire melt pools in order to arrive at dependable melt compositions.

Some experiments show local crystallization of quenched phlogopite at the edges of the melt pools, resulting in strong variations in K_2O contents (Fig. 5, marked in bold text and solid boxes). In other experiments, quenched phlogopite is homogenously distributed throughout the melt pools (italics in Fig. 5). The remaining experiments (Fig. 5) did not show any heterogeneity in quenching across the melt pools, and phlogopite (or carbonate) was not detected as quench phase.

Similar quench features were highlighted by Tumiati et al. (2013) for carbonated K-rich low silicate melt on a single polished surface. Without sectioning at different depths and repolishing of the melt pools, inhomogeneous quench features could remain hidden, so that the melt compositions measured on a single polished section could be falsified drastically, especially for volatile and alkali-rich, silica-poor melts at low degrees of melting.

In multi-anvil experiments, the capsule size was small (~0.4 mm ID), so that a maximum of two layers in melt pools could be analysed. In some multi-anvil run products at 7 GPa, only one exposed layer could be measured due to the small melt pool sizes, so that melt compositions are less certain (Table 3, marked #).

Despite the difficulties inherent in this method, systematic changes in melt composition with pressure and temperature are apparent (Fig. 6), permitting a high degree of confidence in the accuracy of the compositions. Moreover, the use of FE-SEM with short acquisition times (resulting in less destructive analysis of sensitive materials) enabled the detection of quenched vapour as a minor overprint on near solidus melt compositions, such as in HPK and HP experiments (F017-HPK, F001-HP) and vapour quench in sub-solidus run HP009-HP.

4.3. Major element compositions of melts

The generally large standard deviations for melt analyses, in particular SiO_2 (Table 3), reflect the heterogeneity of quenching, which is more

Table 3
Major and minor element compositions [wt%] of melts (and fluid quench).

Experiment	P (GPa)	T (°C)	Phase	Modal abundance (%)	n	SiO2	TiO2	Al2O3	FeO	MnO	MgO	CaO	Na2O	K2O	Cr2O3	P2O5	Total	Mg#	H2O (wt%)	CO2 (wt%)
F001-HPK	2.5	990	melt	6.9	3	14.6(3.9)	0.01(0.03)	0.42(0.12)	5.20(3.52)	0.07(0.10)	12.7(2.3)	17.3(1.8)	1.18(1.51)	0.23(0.40)	0.17(0.12)	4.84(0.6)	56.8(3.6)	83.0	0.4	30.8
E002-HPK	2.5	1090	melt	8.0	2	31.2(5.6)	1.78(0.4)	8.21(1.28)	4.63(0.76)	b.d.l.	6.13(2.18)	7.43(3.19)	1.13(0.65)	2.69(0.57)	0.20(0.00)	0.18(*1)	63.4(9.4)	69.1	11.4	13.2
F015-HPK	2.5	1130	melt	21.1	8	38.5(1.0)	1.41(0.07)	7.81(0.34)	5.88(0.10)	b.d.l.	10.8(0.9)	9.07(0.76)	1.01(0.09)	3.12(0.37)	0.21(0.05)	0.16(0.01)(*3)	77.9(2.3)	74.6	2.8	7.2
F017-HPK	4	*1020*	melt+fluid quench	~7.3	2	23.2(1.2)	1.57(0.5)	5.80(0.16)	4.78(0.17)	0.04(0.05)	8.35(0.02)	12.2(1.2)	0.33(0.04)	4.45(0.20)	0.08(0.06)	0.58(0.39)	61.5(0.6)	75.7	4.9	21.6
F003-HPK	4	1040	melt	6.9	*5*	13.1(3.4)	0.70(0.2)	8.18(2.18)	3.47(0.55)	b.d.l.	10.1(2.4)	12.8(0.7)	0.17(0.03)	6.33(2.34)	0.43(0.15)	0.42(*1)	55.2(2.1)	86.8	18.6	22.7
F004-HPK	4	1090	melt	9.9	16	24.0(10.5)	1.57(1.5)	5.17(2.45)	7.1(3.18)	0.07(0.02)	14.0(2.66)	11.2(7.52)	0.38(0.09)	2.95(2.26)	0.19(0.11)	0.35(0.12)(*5)	69.9(8.76)	78.4	2.8	18.8
F013-HPK	4	1170	melt	17.2	3	35.1(1.9)	1.65(0.1)	7.70(0.96)	6.82(0.59)	b.d.l.	15.4(1.0)	7.00(1.53)	0.51(0.03)	4.66(0.69)	0.40(0.05)	0.03(*1)	79.2(2.4)	80.1	0.7	8.1
HP009-HPK	5	1090	melt	11.7	14	12.5(2.5)	3.06(0.5)	1.84(0.60)	8.22(0.42)	0.11(0.04)	17.8(0.9)	18.3(1.9)	0.53(0.29)	0.75(0.28)	0.12(0.01)	0.26(0.08)(*13)	63.7(3.2)	79.5	0.3	28.9
HP012-HPK	5	1170	melt	14.5	11	17.8(3.5)	3.94(1.1)	3.37(0.98)	10.1(1.5)	0.02(0.00)	17.6(3.2)	16.3(2.7)	0.69(0.22)	1.83(0.30)	0.07(0.07)	0.47(0.49)(*7)	72.0(4.9)	75.6	1.9	19.1
HP012-HPK	5	1170	carb melt	~0.1	4	11.1(7.1)	0.12(0.08)	5.36(3.46)	6.94(1.17)	b.d.l.	12.8(1.7)	23.7(6.1)	0.09(0.12)	0.00(0.03)	0.44(0.27)	0.33(0.13)(*5)	60.6	81.3	0.0	39.0
HP014-HPK	5	1210	melt	21.1	12	19.1(5.6)	2.15(1.3)	3.79(2.52)	9.29(1.69)	b.d.l.	17.8(3.5)	17.3(3.2)	0.60(0.31)	0.85(0.29)	0.17(0.24)	0.15(*1)	70.8(6.7)	77.2	0.5	19.7
MA1163-HPK	7	1210	melt	~14	17	28.7(1.6)	1.22(0.2)	2.72(0.18)	5.62(0.82)	0.01(0.05)	20.0(1.5)	7.91(0.64)	3.06(1.03)	4.28(0.57)	0.20(0.11)	0.03 (*1)	73.8(3.1)	87.4	7.6	24.5
F001-HP	2.5	990	melt+fluid quench	~10.8	17	28.0(4.2)	1.67(1.2)	9.88(2.00)	5.32(1.17)	0.10(0.03)	8.42(3.35)	10.7(2.7)	1.97(0.61)	1.10(0.35)	0.07(0.05)	0.87(0.23)	68.2(4.1)	70.0	0.8	19.0
E002-HP	2.5	1090	melt	13.8	5	37.8(7.2)	1.70(1.5)	11.2(1.8)	6.31(0.96)	b.d.l.	9.75(1.80)	8.90(6.15)	0.59(0.21)	0.42(0.10)	0.19(0.04)	0.18(0.12)	77.1(8.6)	73.2	2.1	8.9
F015-HP	2.5	1130	melt	27.7	8	41.1(0.7)	1.97(0.3)	9.62(0.60)	6.79(0.50)	b.d.l.	14.2(1.2)	10.3(0.9)	1.55(0.26)	0.49(0.12)	0.33(0.06)	0.15(*1)	86.4(1.4)	80.0	2.7	6.4
F003-HP	4	1040	melt	8.1	13	15.8(4.7)	2.25(1.2)	3.73(0.72)	6.73(0.82)	0.02(0.00)	12.5(1.4)	14.9(2.8)	0.96(0.23)	0.86(0.27)	0.10(0.05)	0.36(0.14)	58.2(5.8)	76.9	3.2	26.5
F004-HP	4	1090	melt	9.2	7	19.7(3.1)	1.45(0.7)	4.40(0.64)	7.65(0.55)	b.d.l.	13.2(1.3)	13.5(1.6)	0.73(0.36)	1.30(1.43)	0.21(0.05)	0.23(0.05)(*6)	61.6(5.2)	75.3	1.8	23.9
F013-HP	4	1170	melt	16.8	8	38.5(1.0)	2.66(3.5)	7.81(0.34)	5.88(0.10)	b.d.l.	10.8(0.9)	9.00(0.60)	1.01(0.09)	3.12(0.37)	0.21(0.05)	0.16(0.01)(*3)	79.1(3.7)	74.6	1.3	12.6
HP009-HP	5	1090	fluid quench	~12.4	1	35.0	0.96	7.47	4.56	b.d.l.	15.5	2.92	0.25	6.61	0.21	0.6	82.8	86.2	5.0	5.2
HP014-HP	5	1210	melt	15.3	6	28.6(6.4)	3.71(1.6)	4.03(1.25)	9.78(1.50)	b.d.l.	18.1(1.8)	11.9(2.2)	0.60(0.16)	0.41(0.26)	0.22(0.12)	0.15(*1)	77.3(5.8)	76.6	0.7	15.0
MA1163-HP	7	1210	melt $^{\#}$	~10	6	10.9(4.6)	0.21(0.3)	1.10(0.59)	6.41(2.21)	b.d.l.	15.2(5.8)	21.3(6.3)	1.25(0.19)	0.45(0.10)	0.04(0.10)	0.68(*1)	56.9(6.6)	80.0	1.4	36.7
F005-HZ1	2.5	990	melt	7.4	12	37.4(1.9)	0.42(0.2)	11.9(0.9)	5.39(1.06)	b.d.l.	9.58(3.67)	8.42(3.85)	0.65(0.15)	0.19(0.10)	0.16(0.05)	0.21(0.07)(*8)	83.7(4.6)	75.6	7.3	11.4
E006-HZ1	3.5	1090	melt	22.1	8	44.8(3.4)	0.74(0.1)	12.2(1.7)	6.69(1.05)	b.d.l.	15.0(1.9)	9.86(2.09)	1.70(0.33)	0.35(0.12)	0.29(0.15)	0.51(0.29)(*6)	92.1(4.2)	79.9	1.2	2.7
HP007-HZ1	5	*1140*	melt	3.0	3	29.5(0.9)	0.38(0.1)	4.98(0.22)	5.64(0.88)	b.d.l.	13.4(2.5)	6.98(2.48)	0.49(0.07)	0.14(0.02)	0.24(0.07)	2.1(*1)	61.9(2.7)	80.9	10.2	15.9
HP010-HZ1	5	1170	melt	6.3	*2*	33.9(0.9)	0.15(0.1)	15.0(0.2)	4.62(0.88)	0.17(0.00)	19.5(2.5)	4.21(2.48)	0.25(0.07)	0.23(0.02)	1.29(0.07)	0.13(0.15)(*2)	79.2(2.7)	88.1	3.1	10.7
MA1161-HZ1	7	1170	melt $^{\#}$	~4	8	23.8(5.4)	0.55(0.2)	2.18(0.44)	6.30(1.38)	0.03(0.09)	21.2(1.9)	8.00(4.95)	0.48(0.20)	0.12(0.06)	0.15(0.07)	0.34(0.11)(*5)	23.8(5.4)	83.6	7.6	24.5
MA1163-HZ1	7	1210	melt $^{\#}$	~7	10	24.6(8.1)	1.83(0.9)	2.58(0.84)	6.45(1.67)	0.02(0.05)	19.0(5.6)	13.2(4.3)	1.35(0.58)	0.59(0.17)	0.12(0.13)	0.12(*1)	69.8(8.2)	85.2	3.3	21.9

(continued on next page)

Table 3 (*continued*)

Experiment	P (GPa)	T (°C)	Phase	Modal abundance (%)	n	SiO2	TiO2	Al2O3	FeO	MnO	MgO	CaO	Na2O	K2O	Cr2O3	P2O5	Total	Mg#	H2O (wt%)	CO2 (wt%)
F005-TQ	2.5	990	melt	8.2	14	39.6(1.3)	0.61 (0.05)	13.8(0.4)	6.33(0.26)	b.d.l.	13.2(0.5)	9.25 (0.64)	0.92 (0.11)	0.18 (0.05)	0.23 (0.03)	0.05(0.02) (*5)	84.3(2.6)	83.4	3.9	7.3
HP010-TQ	5	1170	melt	3.3	7	32.2(4.6)	0.15 (0.2)	2.01 (1.63)	4.78(1.10)	b.d.l.	23.2(8.8)	5.71 (5.89)	0.37 (0.14)	0.09 (0.05)	0.23 (0.08)	0.05(0.02 (*6)	68.9 (10.8)	88.6	4.0	20.1
MA1161-TQ	7	1170	melt #	~11	7	34.2 (11.3)	3.70 (2.8)	3.93 (4.81)	7.62(2.88)	b.d.l.	20.4(8.1)	13.1(7.1)	0.47 (0.34)	0.34 (0.37)	0.34 (0.42)	0.8(0.32) (*4)	84.5(9.8)	84.0	1.2	11.7
MA1163-TQ	7	1210	melt #	~5	9	30.0(1.0)	0.39 (0.07)	3.04 (0.13)	6.85(0.11)	0.02 (0.05)	26.3(0.6)	5.39 (0.56)	1.34 (0.22)	0.23 (0.02)	0.27 (0.04)	0.91(*1)	73.8(1.0)	87.5	1.5	19.7

Errors in parentheses are the 2σ of the mean of the rightmost units of replicate analyses; accordingly 14.6(3.9) should be read as 14.6±3.9 [wt.%] SiO2.
carb melt= interstitial carbonate melt; v/fluid quench: vapour/fluid quench; n= number of measurements.
b.d.l. - below detection limits.
*= P2O5 content measured; accordingly 0.18 (*1) should be read as 0.18 [wt%] P2O5 only present in 1 measurement from the total measurement numbers (2).
= only one polished surface were analysed.

marked for incipient and lower degree melts (see also K_2O distribution in Fig. 5). However, the variability of each melt pool is insignificant with respect to the large variations in estimated melt compositions with pressure and temperature across the suite of experiments (Fig. 6). Experimental melts in this study closely resemble direct compositional analogues with carbonatites and ultramafic lamprophyres across the pressure-temperature and compositional range (Table 3, Fig. 7). However, all melts contain larger amounts of volatiles than their surface counterparts and resemble only indirect analogues, referred to here with the prefix 'volatile-rich' (Fig. 9).

At 2.5 GPa, 990 °C, melt compositions in the four peridotite compositions exhibit significant differences despite similar melt fractions (~6.9–10.8%) (triangles in Figs. 6A-F & 7, Table 3). Melts of HPK are dolomitic carbonatite with the lowest SiO_2 content (14.6 wt%) and high $Ca/(Ca + Mg)$ ratio (0.49), and are in general agreement with previous studies on CO_2-bearing compositions (Dalton and Presnall, 1998; Dasgupta et al., 2007; Sweeney, 1994; Wallace and Green, 1988). This melt (F001-HPK) shows moderate concentrations of Na_2O (1.18 wt%), and low K_2O (0.23 wt%), K_2O/Na_2O ratio (0.19) and TiO_2 (0.01 wt%), which can be attributed to phlogopite and pargasite (± ilmenite) buffering these elements between minerals and melt. The HP melt (F001-HP; ~10.8%) with a minor overlap with a quenched vapour-phase is more siliceous (28.0 wt%) and sodic (1.97 wt%) but exhibits a lower $Ca/(Ca + Mg)$ ratio (0.44). This HP melt is also more potassic (1.1 wt %) and titaniferous (1.67 wt%), because phlogopite and ilmenite have been melted out. Given its overlap with a vapour phase, it might be dolomitic carbonatitic, transitional between dolomitic carbonatitic and (olivine) melilititic or (olivine) melilititic in character (Fig. 7B).

Incipient melts of HZ1 (7.4%) are volatile-rich and nephelinitic in character and coexist with amphibole at 2.5 GPa. Melts of HZ1 (7.4%) and TQ (8.2%) show higher SiO_2 contents (37.4–39.6 wt%), whereas the low K_2O (0.19–0.18 wt%), Na_2O (0.65–0.92 wt%) and TiO_2 (0.42–0.61 wt%) reflect the more depleted character of HZ1 and TQ relative to the Hawaiian pyrolite compositions (HPK, HP). $Ca/(Ca + Mg)$ ratios are generally low in HZ1 and TQ melts (0.38–0.14), due to both higher MgO and lower CaO relative to HPK and HP (Fig. 6).

With increasing temperature (towards 1090 °C) at 2.5 GPa, initially volatile-rich carbonatitic (F001-HPK) and carbonatitic-melilititic (F001-HP) melts with very high CO_2/H_2O ratios (~70 and ~ 25.4, respectively) change character abruptly to volatile-rich melilititic (E002-HPK) and nephelinitic (E002-HP) compositions (Fig. 7B) with low CO_2/H_2O ratios (1.2 and 4.2, respectively) as melt fractions increase only little (Tables 2 & 3). The much more potassic character of the 1090 °C HPK melt relative to the 990 °C HPK is also expressed in the considerable higher K_2O/Na_2O ratio (2.4) of the former due to the breakdown of hydrous phases (phlogopite, pargasite) which contribute strongly to the melt. In contrast, the HP melt becomes less potassic and sodic at 1090 °C, forming a volatile-rich nephelinitic melt caused by the increased stability of amphibole and phlogopite.

With a further 50 °C increase in temperature to 1140 °C, the amount of melt increases abruptly (HPK 21.1%, HP 27.7%) as soon as phlogopite (+cpx) (HPK) or amphibole + phlogopite (+ sp) (HP) are melted out. Both melts remain melilititic (F015-HPK) and nephelinitic (F015-HP) with the HPK melt richer in K_2O (3.12 wt% HPK) than the HP melt (0.49 wt%), expressed also in the K_2O/Na_2O ratio, (3.1 for HPK, 0.3 for HP; Table 3, Figs. 6D, 7B).

Near-solidus melts for the enriched HPK and HP compositions have slightly higher SiO_2 contents (Table 3) than were found in previous studies on enriched peridotites (KLB, Dasgupta et al., 2007; HPK and HP, Foley et al., 2009; KNCFMAS+COH, Tumiati et al., 2013) (Fig. 6A). The near-solidus melt compositions may be complicated by small undetected overprints from quenched vapour, but these effects are expected to decrease towards greater mantle depths due to the increasing solubility of H_2O and CO_2 with pressure (Iacono-Marziano et al., 2012).

The near-solidus sodic-potassic dolomitic carbonatite-like HPK melt at 4 GPa 1020 °C (F017-HPK) shows an overlap with a quenched vapour

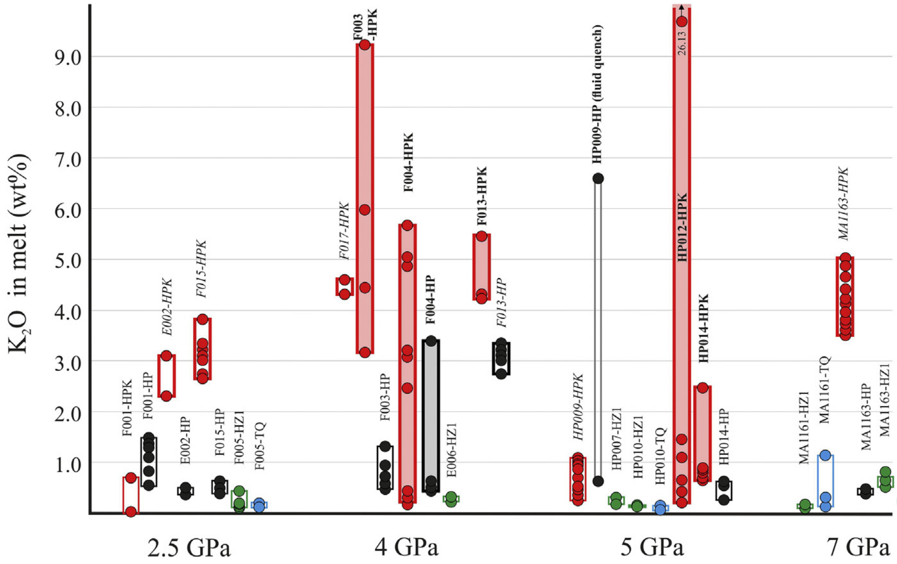

Fig. 5. Measured K_2O content variations in melts. Single measurements are represented with circles (red-HPK, black-HP, green-HZ1, blue-TQ). Italic letters and thick box contours (E002-HPK, F015-HPK, F017HPK, F013-HPK, MA1163-HPK) represent experiments with quenched phlogopite homogenously distributed in the melt pool. Experiments with bold letters and coloured boxes represent heterogeneously quenched phlogopite (crystallized at the edges of the melt pools). (For interpretation of the references to colour in this figure legend, the reader is referred to the web version of this article.)

phase (~7.3%), as observed for F001-HP (see above). At 4 GPa, 1040 °C (F003-HPK, F003-HP), incipient partial melts of HPK and HP are silicate-bearing dolomitic carbonatites (Figs. 6 & 7, Table 3): HPK melts are extremely K-rich ($K_2O/Na_2O = 37.2$), while HP melts are K_2O-poor ($K_2O/Na_2O = 0.9$). As temperatures increase, melts become more siliceous and magnesian before phlogopite is melted out, leading to aillikitic melt compositions (in F004 1090 °C: 9.9% melt in HPK and 9.2% melt in HP; Fig. 7). Here, HPK melts become less potassic, leading to K_2O/Na_2O of only 7.8, while the K_2O content of HP melts increases. Once phlogopite is melted out at ~1170 °C, melt fractions increase abruptly (14.5–16.8% for HPK and HP), and become richer in SiO_2 and less calcic. HPK and HP melts become richer in K_2O, reaching K_2O/Na_2O of 9.1 and 3.1, respectively. HPK melts decrease in $Ca/(Ca + Mg)$, while the $Ca/(Ca + Mg)$ ratio of HP melts remains unchanged (Fig. 6).

While HP is sub-solidus at 5 GPa, 1090 °C, the HPK melt at this pressure and temperature is similar to that at 4 GPa, except that minor carbonate is still stable as a residual phase in addition to phlogopite (Table 2, S2). When these minor phases are melted out, HPK melts evolve to aillikite with a higher K_2O/Na_2O ratio at 1170 °C (2.7) than at 1210 °C (1.4), but remain poorer in silica and possess a higher $Ca/(Ca + Mg)$ ratio than at 4 GPa for a given melt fraction (Fig. 6E). HP melts also evolve to aillikite at 5 GPa, 1210 °C, but with higher SiO_2 and lower K_2O/Na_2O ratio (0.7) than HPK melts at the same pressure. At 1170 °C, in HPK, a small amount of carbonatitic melt was identified trapped between garnet grain clusters (Table 3) adjacent to, but independent of, the main aillikite melt pool.

At 7 GPa, 1210 °C, olivine, orthopyroxene and garnet form the residue in both HPK and HP and coexist with aillikitic (~17%) and dolomitic carbonatite (~10%) melts, respectively. HPK melts have K_2O/Al_2O_3 of 1.6 and at given melt fraction, and become less siliceous towards greater depths (from 2.5 to 5 GPa; Fig. 6A). At 5 GPa, the HP melts are the least siliceous ($SiO_2 = 10.9$ wt%) and display the highest $Ca/(Ca + Mg)$ ratio (0.51) of all melt fractions observed in this study.

Melts of the depleted compositions HZ1 and TQ are generally more enriched in SiO_2 (29.5–44.8 wt%) and depleted in Na_2O (0.25–1.35 wt%) and K_2O (0.09–0.59 wt%) (Table 3). At 2.5 GPa, they have volatile-rich nephelinitic character, whereas at 5–7 GPa, they more closely resemble ultramafic lamprophyre melts with higher MgO contents (13.4–26.29 wt%) (Fig. 7A, B, C). Some melts are kimberlite-like (Fig. 7C) with low K_2O/Na_2O ratios (<0.9). Experimental fluids and melts from a H_2O-CO_2-bearing, K-poor lherzolite (CLZ1; Dvir and Kessel, 2017) in equilibrium with diamond also show ultramafic lamprophyric character with generally lower SiO_2, MgO and higher CaO and volatiles than for HZ1 and TQ melts obtained here (Fig. 7A, C).

4.4. Volatile budget of the melts

At 2.5 GPa, 990 °C, the carbonatitic HPK and HP melts are very rich in CO_2 (~19–30.8 wt%) and have very low H_2O (~0.4–0.8 wt%) because most H_2O is still incorporated in amphibole/phlogopite (Table 2, Fig. 8, Table S2). As temperature increases at 2.5 GPa, the peak H_2O content for HPK melts appears to be reached at 1090 °C (shortly before the complete breakdown of phlogopite at 1130 °C), leading to H_2O- and CO_2-rich melts. The situation for HPK at 4 GPa is similar, although the peak H_2O content (1040 °C) is already reached 130 °C before complete exhaustion of phlogopite (at 1170 °C). Instead, H_2O in HP melts gradually increases at 2.5 GPa and decrease gradually at 4 GPa.

At 2 to 3 GPa, an abrupt change from very low to very high H_2O concentrations was observed where carbonatitic melt coexisting with hydrous phases passes to carbonate-poor melts at higher temperature (HPK in Figs. 8, 9; Wallace and Green, 1988; Green et al., 2014).

For HPK, HP, HZ1 and TQ, the CO_2 content of the melt decreases continuously during partial melting (Fig. 8A, Table 3).

5. Discussion

5.1. Near-solidus melt compositions

The differences in peridotitic starting compositions (HPK, HP, HZ1, TQ) and their initial volatile contents (2.88–0.3 wt% CO_2, 0.58–0.3 wt% H_2O) allows generalized conclusions about the evolution of melt compositions across pressure and temperature in the incipient melting regime in the mantle. The temperature region of carbonatitic melt stability is wide (~250 °C) at ~2.1- ~ 3 GPa, where carbonatitic melt coexists with amphibole and phlogopite-bearing peridotite (Green, 2015; this study). Melt is mainly dolomitic in character with high $Ca/(Ca + Mg)$ ratios in fertile pyrolitic compositions (HPK and HP), very poor in

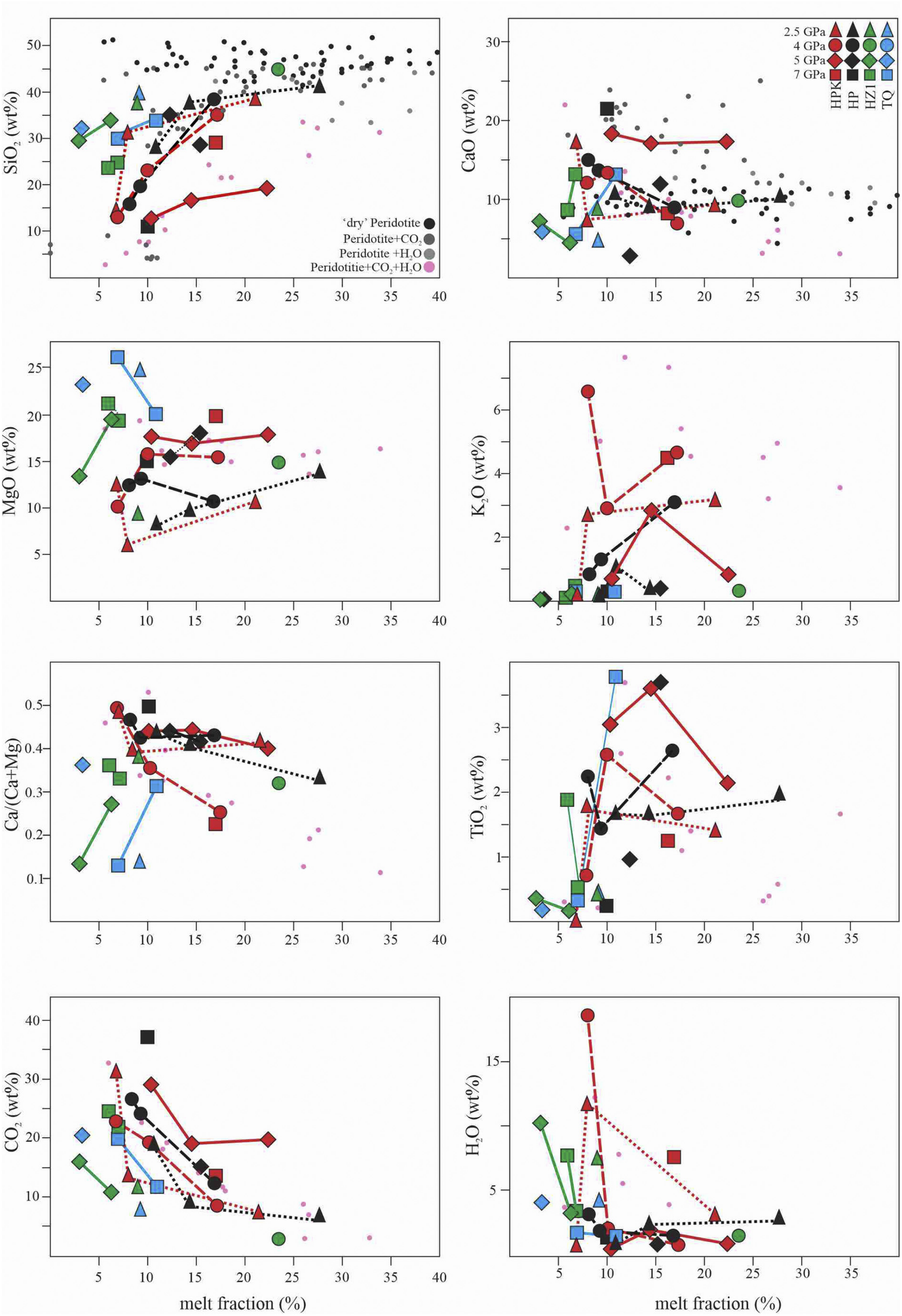
SiO$_2$ (wt%)
'dry' Peridotite ●
Peridotite+CO$_2$ ●
Peridotite +H$_2$O ●
Peridotitie+CO$_2$+H$_2$O ●
CaO (wt%)
2.5 GPa
4 GPa
5 GPa
7 GPa
HPK
HP
HZ1
TQ
MgO (wt%)
K$_2$O (wt%)
Ca/(Ca+Mg)
TiO$_2$ (wt%)
CO$_2$ (wt%)
H$_2$O (wt%)
melt fraction (%)
melt fraction (%)

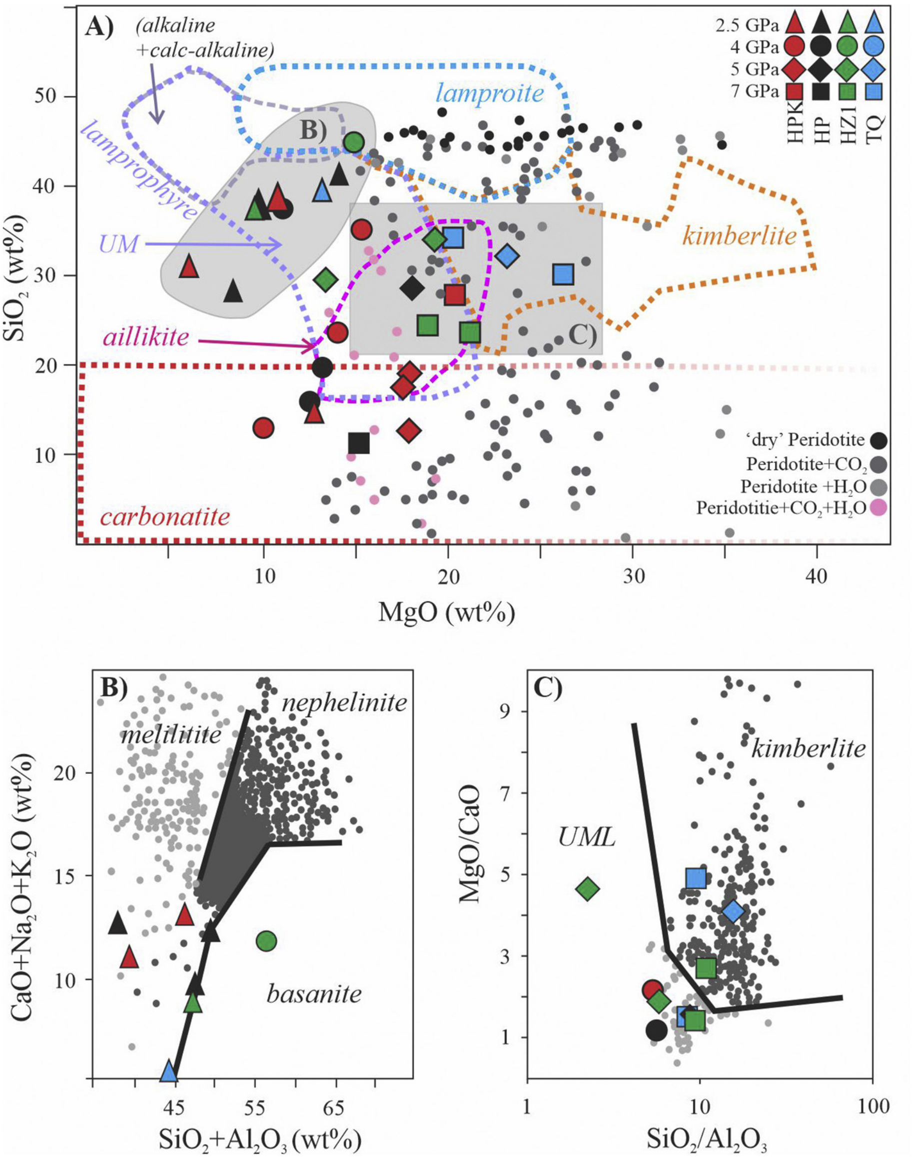

Fig. 7. Compositions and nomenclature of the experimental incipient and low degree melts (2.5–7 GPa). (A) SiO_2 versus MgO (wt%) discrimination diagram with compositional fields for natural carbonatite, aillikite, alkaline lamprophyre, lamproite and kimberlite and aillikite fields based on Rock (1991),Lefebvre et al. (2005) and Tappe et al. (2006). Small circles are previous experimental melts from peridotitic systems in presence of CO_2-H_2O (Foley et al., 2009; Tumiati et al., 2013), peridotite+CO_2 (Dasgupta et al., 2007, 2013; Dasgupta and Hirschmann, 2007), 'dry' peridotite (Hirose & Kushiro, 1993; Walter, 1998), peridotite+H_2O (Kawamoto & Holloway, 1997; Tenner et al., 2012, Green et al., 2014); (B) Experimental melts at 2.5–3.5 GPa 1090 and 1130 °C compared to melilitite, nephelinite and basanite fields (Le Bas, 1989; datasets from GEOROC database, http://georoc.mpch-mainz.gwdg.de). (C) HZ1 and TQ experimental melts in MgO/CaO versus SiO_2/Al_2O_3 diagram, which discriminates natural ultramafic lamprophyre and kimberlite (Rock, 1991; datasets from GEOROC database, http://georoc.mpch-mainz.gwdg.de). (For interpretation of the references to colour in this figure legend, the reader is referred to the web version of this article.)

H_2O but very high in CO_2/H_2O ratios (Fig. 8). The width of the carbonatite melt field is strongly dependent on the dehydration of amphibole and phlogopite, which have different compositions depending on the peridotite involved (Wallace and Green, 1988; Foley et al., 2009; Green et al., 2010, 2014; Green, 2015; this study; Fig. 9). Interestingly, Tumiati et al. (2013) reported sub-solidus conditions in the model mantle composition KNCFMAS+COH at similar pressure, temperature (2.6 GPa 900–1040 °C) and oxygen fugacity (fO_2) conditions, with carbonate as a solid phase in equilibrium with graphite and CO_2-H_2O fluids in amphibole-phlogopite-bearing peridotite. Probably, the higher solidus in this simplified peridotitic composition is explained by higher Al_2O_3, CaO, and alkalis, lower FeO, and the lack of TiO_2, Cr_2O_3, MnO and NiO.

Within a temperature interval of ~100 °C from 990 to 1090 °C at 2.5 GPa in this study, melts become much more siliceous, potassic (HPK only) and hydrous, but less calcic, evolving to volatile-rich melilitite (HPK) and volatile-rich nephelinite (HP) compositions. This change is caused by enhanced breakdown of hydrous phases and addition of their components to the carbonatitic melt, resulting in strong increases in SiO_2, K_2O (HPK only), TiO_2, and H_2O, and decreases in CaO, MgO (HPK only), Ca/(Ca + Mg) and CO_2 (Figs. 6A-H, 8,9). These melts contain a larger amount of volatiles than their surface counterparts (Fig. 8B),

Fig. 6. Variations in melt compositions in HPK, HP, HZ1 and TQ experiments as a function of pressure (see key) and melt fraction. Small circles are previous experimental melts from peridotitic systems in presence of CO_2-H_2O (Foley et al., 2009), peridotite+CO_2 (Dasgupta et al., 2007, 2013; Dasgupta and Hirschmann, 2007), 'dry' peridotite (Hirose & Kushiro, 1993; Walter, 1998), peridotite+H_2O (Kawamoto & Holloway, 1997).

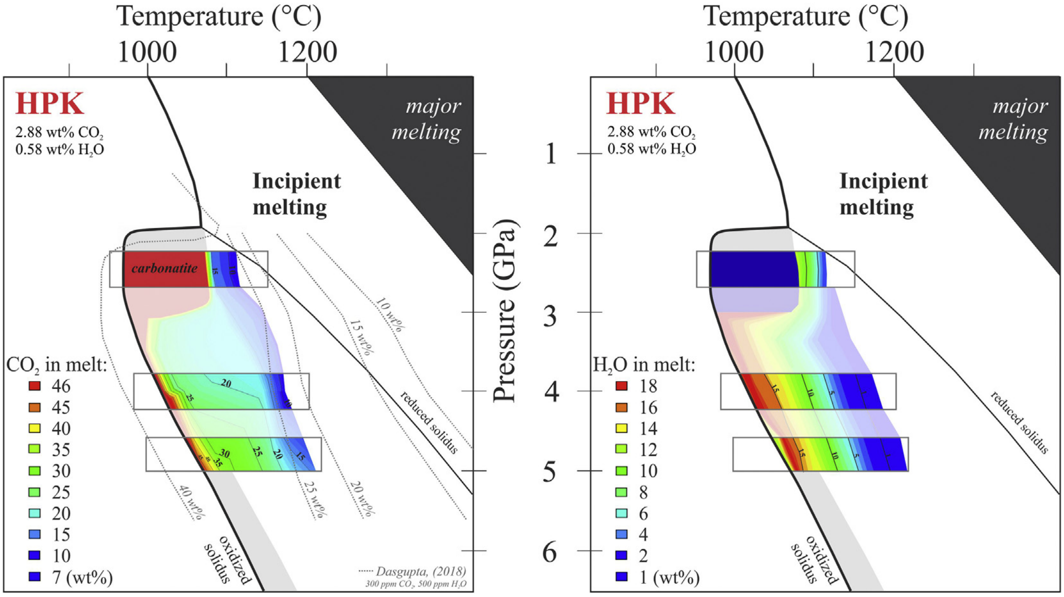

Fig. 8. CO_2 and H_2O contents of experimental melts at various pressures and temperatures in the incipient melt region for K-enriched Hawaiian pyrolite (HPK) with 2.88 wt% CO_2 and 0.58 wt% H_2O compared to the oxidized solidus in the CO_2-H_2O-peridotite system. The coloured areas show the estimated CO_2-contents of melts of this study at 2.5, 4 and 5 GPa. Melt compositions between these pressures are interpolated in more transparent shading. Black lines are isopleths at given CO_2-contents of melts. Grey dotted lines indicate the CO_2-in-melt isopleths from Dasgupta (2018) for peridotite+CO_2 + H_2O (300 ppm CO_2, 500 ppm H_2O). Melting curves for peridotite+CO_2 + H_2O in oxidized conditions (after Foley et al., 2009) and for peridotite with CH_4 + H_2O in reduced conditions are indicated with black lines. Position of major melting regime after Green (2015) and references therein. Grey area is the estimated carbonatitic melt field after Foley (2008). (For interpretation of the references to colour in this figure legend, the reader is referred to the web version of this article.)

and are therefore referred to here as volatile-rich nephelinite and volatile-rich melilitite. As temperatures increase further (1090 to 1130 °C), the complete breakdown of hydrous phases causes melt compositions to change continuously to become more siliceous, less calcic and less volatile-rich (Fig. 6A, B, G, H).

The carbonatitic melt field narrows in temperature range (~90–100 °C) at pressures above 3 GPa, and our results show it to be more restricted than previously discussed (Dasgupta, 2018; Foley et al., 2009), probably because HPK and HP contain less H_2O and CO_2 in our study, resulting in the quicker breakdown of both carbonate and phlogopite.

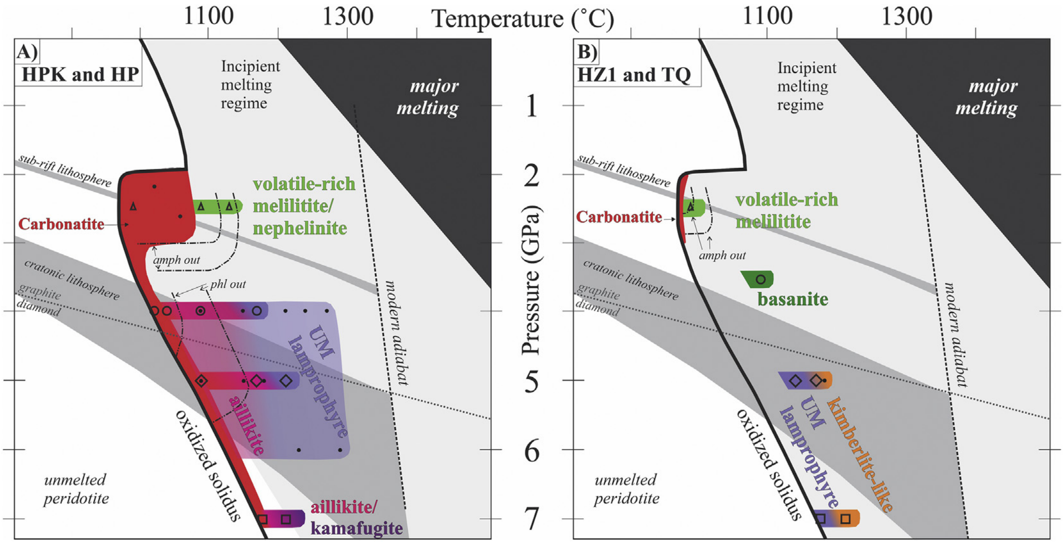

Fig. 9. Application of the experimentally determined melt compositions in presence of CO_2 and H_2O as a model for melting of continental, cratonic, sub-lithospheric and asthenospheric mantle. (A) Melts from enriched compositions HPK, HP (this study) and 95% HZ1 + 5 wt% anhydrous phlogopite (Green et al., 2014); amphibole stability limit extends to a maximum of ~3.2 GPa based on HPK (+CO_2 + H_2O) composition after Wallace and Green, 1988, Wallace and Green, 1991) and ~ 3 GPa for HP (+CO_2 + H_2O) composition (Green, 2015 and references therein). Phlogopite stability limit extends to a maximum of 4.5 GPa based on HP + CO_2 + H_2O (this study), and ~ 5.5 GPa based on HPK + CO_2 + H_2O (this study). Phlogopite out towards higher temperature based on Foley et al. (2009), 95% HZ1 + 5 wt% anhydrous phlogopite +1.45 wt% H_2O (Green et al., 2014), and this study. (B) melts from volatile-saturated, unmetasomatized compositions (HZ1, TQ); amphibole stability limit extends to ~2.8 GPa for HZ1 and ~ 2.5 GPa for TQ compositions (Green, 2015 and references therein). Open symbols = melts from this study (symbols as in Fig. 6); solid circles = experimental partial melts from peridotite+CO_2 + H_2O systems (Wallace and Green, 1988; Foley et al., 2009; Tumiati et al., 2013). The sub-rift lithosphere geotherm is appropriate for old oceanic lithosphere or young continental rift areas and traverses the wide region of the carbonatite stability field. The presence or absence of carbonatitic HPK and HP melt at >3 GPa and T < 1000 °C depends on the presence or absence of excess CO_2 and on local variations of fO_2. Further melting is controlled at T > 1000 °C by the stability of calcic amphibole, phlogopite and carbonatite melts. The cratonic lithosphere geotherm (~30–50 mW/m^2 after Tappert and Tappert, 2011) may intersect the oxidized solidus (CO_2 + H_2O) only if deep cratonic mantle/asthenospheric regions are oxidized and carbonate is present. (For interpretation of the references to colour in this figure legend, the reader is referred to the web version of this article.)

At 4 and 5 GPa, phlogopite remains the sole hydrous phase near the solidus of HPK, and silicate-bearing dolomitic carbonatites develop into more siliceous and magnesian melts (aillikitic; Tappe et al., 2006) within a relatively small temperature interval (25–50 °C). The lowest degree HPK melts at 4 GPa (1020 and 1040 °C) are alkali-rich dolomitic carbonatite in character with high K_2O (4.45–6.33 wt%), H_2O (~4.9–18.6) and CO_2 contents (~21.6–22.7 wt%) (Figs. 6D, G, H, 8, 9A, Table 3). SiO_2 gradually increases with increasing temperature in HPK melts as Ca/(Ca + Mg) ratios decrease (Fig. 6A, E) forming hydrous carbonate-bearing aillikites and ultramafic lamprophyre (Figs. 7A, 9A, Foley et al., 2009; this study). In contrast, phlogopite remains a residual phase up to 4 GPa only in HP, and silicate-bearing dolomitic carbonatites progress to ultramafic lamprophyres once phlogopite is melted out (Fig. 7, Table 3). Melting of phlogopite (~1150–1180 °C; Foley et al., 2009) leads to strong K-enrichment with concomitant H_2O-enrichment over a limited temperature range (Figs. 8B, 9A) in the SiO_2-poor carbonatitic/ultramafic melt, as described in previous studies (Sweeney, 1994; Thibault et al., 1992; Foley et al., 2009; this study).

At 7 GPa, in the HP experiment with low melt fraction (~10%), melt compositions are dolomitic carbonatite similar to those at lower pressures (4–5 GPa) (Figs. 6, 7). In the HPK experiments, the melt fraction is larger (~17%) and melts are more enriched in potassium (4.28 wt%), resembling kamafugites (Fig. 9A, Rosenthal et al., 2009). Melts of the depleted compositions (HZ1, TQ) are generally richer in Si and Mg than in HPK and HP at similar conditions. The incipient melts are volatile-rich nephelinitic to ultramafic lamprophyre-kimberlite-like in character with high volatile contents (~24.5–11.7 wt%) (Fig. 9B). Low-degree melts of HZ1 are volatile-rich nephelinitic at 2.5 GPa in equilibrium with amphibole, and progress with increasing MgO (9.58–21.2 wt%) towards deeper mantle levels to ultramafic lamprophyre/kimberlite-like at 7 GPa (Figs. 7C, 8, 9A). These melts resemble kimberlites in terms of MgO/CaO and SiO_2/Al_2O_3, but Na and K are more depleted than kimberlites (Fig. 7A, C; Foley et al., 2019).

Melts of TQ show lower SiO_2, MgO, FeO and Cr_2O_3 contents compared to low-degree melts of volatile-free TQ at 2–3 GPa (Falloon et al., 1988), with a similar range of CaO and Na_2O but higher K_2O. At 5–7 GPa, low degree melts are more MgO-rich (20.4–26.3 wt%), similar to ultramafic lamprophyres and trending towards kimberlite-like in character (Figs. 7C, 9B).

5.2. Application to petrogenesis of silica-undersaturated magmas in the upper mantle

The pressure range of 4–7 GPa is thought to be relevant for the generation of carbonatites, aillikites, ultramafic lamprophyres, kamafugites, olivine melilitites, and possibly kimberlites, all of which require the volatiles CO_2 and H_2O.

Our results agree with previous studies in that natural magmas found at the Earth's surface do not resemble the primary experimental melts from volatile-bearing upper mantle peridotites. The latter are considerably less enriched in trace elements than surface carbonatites (Rudnick et al., 1993; Yaxley et al., 1991), and considerably more enriched in volatiles. The experimental melts are therefore referred to here with the prefix ‘volatile-rich’ as in volatile-rich nephelinite and volatile-rich melilitite (Figs. 7, 9).

The experimentally produced incipient melts from the enriched compositions HPK and HP indicate a genetically related series between carbonatitic and ultramafic lamprophyric (particularly aillikitic) melts with increasing pressure and temperature (Brey, 1978; Dalton and Presnall, 1998; Tappe et al., 2006, Litasov et al., 2008; Foley et al., 2009; Keller and Katz, 2016; this study; Fig. 7). These melts show no strong increase in MgO with greater mantle depth and are enriched in CO_2, H_2O and potassium over a restricted temperature range (~100 °C), indicating that these chemical characteristics might be generated during melting (Dasgupta, 2018; Foley et al., 2009) (Fig. 9A).

In contrast, melts of HZ1 and TQ generally show high MgO contents and similarities in SiO_2, Al_2O_3, and CaO contents to kimberlites (Fig. 7C). The source regions of kimberlites may include a depleted ultramafic assemblage (Pasteris, 1984) with H_2O and CO_2 (Kjarsgaard et al., 2009), but no experimental melts of peridotite with H_2O and CO_2 replicate the high K_2O/Na_2O ratios observed in Group I kimberlites (Fig. 9B, Foley et al., 2019). The 7 GPa melts described here for HZ1 and TQ may correspond to the initial melts that lead to kimberlites after enrichment in alkalis and carbonate through reaction at the base of the lithosphere as hypothesized by Foley et al. (2019).

Incipient melting may occur below the base of cold, thick cratons (~4–7 GPa) where the presence of $CO_2 + H_2O$ (in oxidized conditions) depresses the melting point of peridotite in a limited pressure-temperature region into conditions corresponding to lower geothermal gradients (Fig. 9A-B, Foley, 2008; Foley et al., 2009; Guex et al., 2016; Foley and Pintér, 2018; this study). The asthenosphere below cratonic areas may still be locally oxidized with minor carbonate and phlogopite in peridotite but this may be limited to local patches because most of the lower cratons may be more reduced at these great depths (Frost and McCammon, 2008; Stagno et al., 2013). Local melting of these oxidized rocks associated with upwelling mantle and/or plume activity below the cratons (Foley and Fischer, 2017; Sun and Dasgupta, 2019) could produce CO_2-H_2O-rich silica-poor melts.

These oxidized, carbonate-bearing ultramafic patches could be locally established by earlier influx of incipient melts from the volatile-richer asthenosphere (Foley, 2008; Foley and Fischer, 2017). These melts may play important roles either directly as parental melts to magma types such as ultramafic lamprophyres (Foley et al., 2009), or indirectly, forming distinct metasomatic veins (see Section 5.3). The high MgO, CO_2, H_2O and K_2O/Na_2O ratios of kimberlites may result from the interaction of asthenospheric melts with this metasomatised lower lithosphere, producing a mixed source signature (Foley et al., 2019).

The source regions of kamafugites, ultramafic lamprophyres and kimberlites have probably experienced multi-stage metasomatic overprints caused by solidification of incipient melts at depth, followed by reactivation via melting; this is frequently suggested to explain radiogenic isotope signatures (Andronikov and Foley, 2001; Rosenthal et al., 2009; Tappe et al., 2006).

5.3. Application to metasomatism in the upper mantle

Incipient mantle melts are important not only directly for the production of parental melts to some magma types, but also indirectly as agents of metasomatism due to the potential of incipient melts to transport large amounts of volatiles, Na and K through the upper mantle. Mantle metasomatism is defined as a compositional change in mantle rocks due to interaction with mantle fluids or melts. However, in most cases, the metasomatic reactions observed in mantle xenoliths are complete, so that the metasomatic agent can only be inferred, but not observed directly (O'Reilly and Griffin, 2013).

At shallow depths (2.5 GPa, Fig. 9A), a sub-rift lithospheric geotherm intercepts the wide carbonatitic melt field (~250 °C), where dolomitic carbonatite melt is in equilibrium with phlogopite/amphibole-bearing peridotite. Only a small number of mantle peridotites have been found to store carbonate as direct evidence of the former presence of carbonate melt (Ionov et al., 2018). In the majority of cases, the carbonatitic melt is exhausted by the formation of clinopyroxene and the loss of CO_2, as displayed, for example, in mantle xenoliths from western Victoria (Australia) (O'Reilly and Griffin, 1988; Stolz and Davies, 1988; Yaxley et al., 1991).

Under conditions of the lower cratonic lithosphere (4–7 GPa) progressive metasomatic overprints in cratonic xenoliths, sampled by kimberlites across the world, have been extensively studied (O'Reilly and Griffin, 2013). Many of these effects may be caused by melts similar to those produced in the current experiments. Chemical tomographic studies highlight the complex nature of the bottom of the cratonic lithosphere (O'Reilly and Griffin, 2013), which was produced by episodic infiltration of asthenospheric melt forming extensive metasomatic rock assemblages from phlogopite (±K-richterite)-bearing peridotites to phlogopite-bearing wehrlites and pyroxenites (Konzett et al., 2000). The mineralogy of the metasomatic assemblages is strongly dependent on the compositions of the infiltrating incipient melts. Various metasomatic assemblages with carbonates, clinopyroxene and phlogopite are described as a source for potassium-rich aillikite melt production (Ionov et al., 2018; Tappe et al., 2006). Megacrystalline lherzolites from the Slave craton, Canada, originating from ~6 GPa and ~ 1200–1250 °C contain a wide range of melt inclusions containing calcite, olivine, and mica in carbonatitic to Ca-Mg-silicic matrices corresponding to bulk compositions ranging from Ca-rich carbonatite to Mg-silicate melts (van Achterbergh et al., 2004). The presence of CO_2- and H_2O-bearing alkali-rich, silica-poor fluxing agents indicate that incipient melting at the base of the cratonic lithosphere may be widespread wherever an oxidized solidus applies, as shown by melt inclusions in cratonic xenoliths (Golovin et al., 2018).

However, the presence or absence of carbonatitic melt at >95 km depth will depend on local variations in the oxygen fugacity (fO_2). The cratonic lithosphere geotherm will intersect the oxidized solidus ($CO_2 + H_2O$) only if the deep cratonic mantle/asthenospheric region is oxidized and carbonate is present (Foley, 2011; Fig. 9A-B). Asthenospheric melts or incipient melts from locally oxidized peridotite may become trapped in reduced lower cratonic lithosphere to form diamond-bearing assemblages by redox freezing (Rohrbach and Schmidt, 2011). Fibrous lithospheric inclusions in diamonds preserve multi-phase micro-inclusions of dolomite, phlogopite, (±Fe-oxide, rutile, magnetite, Fe-sulfides) and a hydrous fluid phase (Klein-BenDavid et al., 2009; Kopylova et al., 2010; Logvinova et al., 2019; Zedgenizov et al., 2007). These inclusions resemble the experimentally determined hydrous magnesian carbonatitic melts, commonly with high K contents. These asthenospheric incipient melts are likely to freeze in the base of the cratonic lithosphere forming distinct veins consisting of hydrous phases (phlogopite, K-richterite), carbonates, Fe—Ti oxide minerals and apatite, depending on the composition of the incipient melt.

6. Conclusions

In this systematic high pressure and temperature experimental study we have determined the chemical compositions of incipient melts along the oxidized solidus of four mantle peridotites containing both CO_2 and H_2O between 2.5 and 7 GPa. For fertile peridotite compositions HPK and HP, melts are initially carbonatitic at 2.5 GPa, but pass abruptly to volatile-rich melilititic and volatile-rich nephelinitic compositions at higher degrees of melting, governed by the dehydration melting of hydrous phases. At higher pressures (4–7 GPa) melts progress gradually from carbonatitic to carbonate-bearing silicate melts similar to aillikites over a restricted temperature range of only ~100 °C. Melts of more depleted starting compositions (HZ1, TQ) are richer in silica, showing volatile-rich nephelinitic compositions at 2.5 GPa, and compositions similar to ultramafic lamprophyre and kimberlite-like at 5–7 GPa.

Incipient melts may be important directly as the parental melts of carbonatites, ultramafic lamprophyres, kamafugites, melilitites, nephelinites and possibly kimberlites, and indirectly as agents of metasomatism due to their potential to transport large amounts of volatiles, Na, K in the upper mantle. These incipient melts cause refertilization of the lower regions of the lithosphere, which may be especially extensive in the lower cratonic lithosphere due to the long history of cratons.

Declaration of Competing Interest

The authors declare that they have no known competing financial interests or personal relationships that could have appeared to influence the work reported in this paper.

Acknowledgments

We thank Dean Scott, and Nick Farmer for support with the ultrahigh pressure piston-cylinder apparatuses at RSES, and Jeff Chen, Frank Brink and Hua Chen of the Centre for Advanced Microscopy at ANU for help with the SEM and electronprobe microanalyser. The LA-ICMPS data were obtained using instrumentation funded by DEST Systemic Infrastructure Grants, ARC LIEF, NCRIS/AuScope, industry partners and Macquarie University. This work is supported by the Australian Research Council Centre of Excellence for Core to Crust Fluid Systems CE1101017, ARC grant FL1800134, and a Macquarie University Higher Degree research scholarship to Zs. Pintér. This is contribution 1657 from the ARC Centre of Excellence for Core to Crust Fluid Systems (http://www.ccfs.mq.edu.au) and 1458 in the GEMOC Key Centre (http://www.gemoc.mq.edu.au). We thank the two anonymous reviewers for their constructive reviews and editor Michael Roden for his gracious editorial handling.

Appendix A. Supplementary data

Supplementary data to this article can be found online at https://doi.org/10.1016/j.lithos.2021.106224.

References

Andronikov, A.V., Foley, S.F., 2001. Trace element and Nd–Sr isotopic composition of ultramafic lamprophyres from the East Antarctic Beaver Lake area. Chem. Geol. 175 (3–4), 291–305.

Brey, G., 1978. Origin of olivine melilitites—chemical and experimental constraints. J. Volcanol. Geotherm. Res. 3 (1–2), 61–88.

Brey, G.P., Bulatov, V.K., Girnis, A.V., 2009. Influence of water and fluorine on melting of carbonated peridotite at 6 and 10 GPa. Lithos 112, 249–259.

Dalton, J.A., Presnall, D.C., 1998. The continuum of primary carbonatitic–kimberlitic melt compositions in equilibrium with lherzolite: data from the system CaO–MgO–Al_2O_3–SiO_2–CO_2 at 6 GPa. J. Petrol. 39, 1953–1964.

Dasgupta, R., 2018. Volatile-bearing partial melts beneath oceans and continents–Where, how much, and of what compositions? Am. J. Sci. 318 (1), 141–165.

Dasgupta, R., Hirschmann, M.M., 2006. Melting in the Earth's deep upper mantle caused by carbon dioxide. Nature 440, 659–662.

Dasgupta, R., Hirschmann, M.M., 2007. A modified iterative sandwich method for determination of near-solidus partial melt compositions. II. Application to determination of near-solidus melt compositions of carbonated peridotite. Contrib. Mineral. Petrol. 154, 647–661.

Dasgupta, R., Hirschmann, M.M., Smith, N.D., 2007. Partial melting experiments of peridotite + CO_2 at 3 GPa and genesis of Alkalic Ocean Island Basalts. J. Petrol. 48, 2093–2124.

Dasgupta, R., Mallik, A., Tsuno, K., Withers, A.C., Hirth, G., Hirschmann, M.M., 2013. Carbon-dioxide-rich silicate melt in the Earth's upper mantle. Nature 493 (7431), 211–215.

Demouchy, S., Bolfan-Casanova, N., 2016. Distribution and transport of hydrogen in the lithospheric mantle: a review. Lithos 240, 402–425.

Demouchy, S., Mackwell, S., 2006. Mechanisms of hydrogen incorporation and diffusion in iron-bearing olivine. Phys. Chem. Miner. 33, 347–355.

Dvir, O., Kessel, R., 2017. The effect of CO2 on the water-saturated solidus of K-poor peridotite between 4 and 6 GPa. Geochim. Cosmochim. Acta 206, 184–200.

Eggler, D.H., 1978. The effect of CO_2 upon partial melting of peridotite in the system Na_2O-CaO-Al_2O_3-MgO-SiO_2-CO_2 to 35 kb, with an analysis of melting in a peridotite-H_2O-CO_2 system. Am. J. Sci. 278 (3), 305–343.

Falloon, T.J., Green, D.H., Hatton, C.J., Harris, K.L., 1988. Anhydrous partial melting of a fertile and depleted peridotite from 2 to 30 kb and application to basalt petrogenesis. J. Petrol. 29 (6), 1257–1282.

Falloon, T.J., Green, D.H., Danyushevsky, L.V., McNeill, A.W., 2008. The composition of near-solidus partial melts of fertile peridotite at 1 and 1.5 GPa: Implications for the petrogenesis of MORB. J. Petrol. 49, 591–613.

Foley, S.F., 2008. Rejuvenation and erosion of the cratonic lithosphere. Nat. Geosci. 1, 503–510.

Foley, S.F., 2011. A reappraisal of redox melting in the Earth's mantle as a function of tectonic setting and time. J. Petrol. 52, 1363–1391.

Foley, S.F., Fischer, T.P., 2017. An essential role for continental rifts and lithosphere in the deep carbon cycle. Nat. Geosci. 10 (12), 897.

Foley, S.F., Pintér, Z., 2018. Primary melt compositions in the Earth's mantle. Magmas Under Pressure, pp. 3–42.

Foley, S., Yaxley, G., Rosenthal, A., Buhre, S., Kiseeva, E., Rapp, R., Jacob, D., 2009. The composition of near-solidus melts of peridotite in the presence of CO_2 and H_2O between 40 and 60 kbar. Lithos 112, 274–283.

Foley, S.F., Yaxley, G.M., Kjarsgaard, B.A., 2019. Kimberlites from source to surface: insights from experiments. Elements 15 (6), 393–398.

Frost, D.J., McCammon, C.A., 2008. The redox state of Earth's mantle. Annu. Rev. Earth Planet. Sci. 36, 389–420.

Ghosh, S., Litasov, K., Ohtani, E., 2014. Phase relations and melting of carbonated peridotite between 10 and 20 GPa: a proxy for alkali-and CO_2-rich silicate melts in the deep mantle. Contrib. Mineral. Petrol. 167 (2), 964.

Golovin, A.V., Sharygin, I.S., Kamenetsky, V.S., Korsakov, A., Yaxley, G.M., 2018. Alkali-carbonate melts from the base of the cratonic lithospheric mantle: links to kimberlites. Chem. Geol. 483, 261–274.

Green, D., 1973. Contrasted melting relations in a pyrolite upper mantle under mid-oceanic ridge, stable crust and island arc environments. Tectonophysics 17, 285–297.

Green, D.H., 1976. Experimental testing of "equilibrium" partial melting of peridotite under water-saturated, high-pressure conditions. Can. Mineral. 14, 255–268.

Green, D.H., 2015. Experimental petrology of peridotites, including effects of water and carbon on melting in the Earth's upper mantle. Phys. Chem. Miner. 42 (2), 95–122.

Green, D.H., Hibberson, W.O., Kovács, I., Rosenthal, A., 2010. Water and its influence on the lithosphere-asthenosphere boundary. Nature 467, 448–451.

Green, D.H., Hibberson, W.O., Rosenthal, A., Kovács, I., Yaxley, G.M., Falloon, T.J., Brink, F., 2014. Experimental study of the influence of water on melting and phase assemblages in the upper mantle. J. Petrol. 55, 2067–2096.

Guex, J., Pilet, S., Müntener, O., 2016. Thermal erosion of cratonic lithosphere as a potential trigger for mass-extinction. Sci. Rep. 6, 23168.

Hart, S.R., Zindler, A., 1986. In search of a bulk-Earth composition. Chem. Geol. 57 (3-4), 247–267.

Hermann, J., O'Neill, H.StC., Berry, A.J., 2005. Titanium solubility in olivine in the system TiO2- MgO-SiO2: no evidence for an ultra-deep origin of Ti-bearing olivine. Contrib. Mineral. Petrol. 148, 746–760.

Hernlund, J., Leinenweber, K., Locke, D., Tyburczy, J.A., 2006. A numerical model for steady-state temperature distributions in solid-medium high-pressure cell assemblies. Am. Mineral. 91, 295–305.

Hirose, K., Kushiro, I., 1993. Partial melting of dry peridotites at high pressures: determination of compositions of melts segregated from peridotite using aggregates of diamond. Earth Planet. Sci. Lett. 114 (4), 477–489.

Iacono-Marziano, G., Morizet, Y., Le Trong, E., Gaillard, F., 2012. New experimental data and semi-empirical parameterization of H_2O–CO_2 solubility in mafic melts. Geochim. Cosmochim. Acta 97, 1–23.

Ionov, D.A., Doucet, L.S., Xu, Y., Golovin, A.V., Oleinikov, O.B., 2018. Reworking of Archean mantle in the NE Siberian craton by carbonatite and silicate melt metasomatism: evidence from a carbonate-bearing, dunite-to-websterite xenolith suite from the Obnazhennaya kimberlite. Geochim. Cosmochim. Acta 224, 132–153.

Kawamoto, T., Holloway, J.R., 1997. Melting temperature and partial melt chemistry of H2O-saturated mantle peridotite to 11 gigapascals. Science 276 (5310), 240–243.

Keller, T., Katz, R.F., 2016. The role of volatiles in reactive melt transport in the asthenosphere. J. Petrol. 57 (6), 1073–1108.

Kjarsgaard, B.A., Pearson, D.G., Tappe, S., Nowell, G.M., Dowall, D.P., 2009. Geochemistry of hypabyssal kimberlites from Lac de Gras, Canada: Comparisons to a global database and applications to the parent magma problem. Lithos 112 (1), 236–248.

Klein-BenDavid, O., Logvinova, A.M., Schrauder, M., Spetius, Z.V., Weiss, Y., Hauri, E.H., Kaminsky, F.V., Sobolev, N.V., Navon, O., 2009. High-Mg carbonatitic microinclusions in some Yakutian diamonds—a new type of diamond-forming fluid. Lithos 112, 648–659.

Konzett, J., Armstrong, R.A., Günther, D., 2000. Modal metasoamtism in the Kaapvaal craton lithosphere: constraints on timing and geneiss from U-Pb zircon dating of metasomatized peridotites and MARID-type xenoliths. Contrib. Mineral. Petrol. 139, 704–719.

Kopylova, M., Navon, O., Dubrovinsky, L., Khachatryan, G., 2010. Carbonatitic mineralogy of natural diamond-forming fluids. Earth Planet. Sci. Lett. 291 (1–4), 126–137.

Le Bas, M.J., 1989. Nephelinitic and basanitic rocks. J. Petrol. 30 (5), 1299–1312.

Lefebvre, N., Kopylova, M., Kivi, K., 2005. Archaean calc-alkaline lamprophyres of Wawa, Ontario, Canada: Unconventional diamondiferous volcaniclastic rocks. Precambrian Res. 138, 57–87.

Leinenweber, K.D., Tyburczy, J.A., Sharp, T.G., Soignard, E., Diedrich, T., Petuskey, W.B., Wang, Y., Mosenfelder, J.L., 2012. Cell assemblies for reproducible multi-anvil experiments (the COMPRES assemblies). Am. Mineral. 97 (2–3), 353–368.

Litasov, K.D., Fei, Y., Ohtani, E., Kuribayashi, T., Funakoshi, K., 2008. Thermal equation of state of magnesite to 32GPa and 2073K. Phys. Earth Planet. Inter. 168, 191–203.

Litasov, K.D., Shatskiy, A., Corresponding Member of the RAS Pokhilenko, N. P, 2011. Phase relations and melting in the systems of peridotite-H_2O-CO_2 and eclogite-H_2O-CO_2 at pressures up to 27 GPa. Dokl. Earth Sci. 437 (2), 498–502.

Litasov, K.D., Shatskiy, A., Ohtani, E., 2014. Melting and subsolidus phase relations in peridotite and eclogite systems with reduced C-O-H fluid at 3-16 GPa. Earth Planet. Sci. Lett. 391, 87–99.

Logvinova, A., Zedgenizov, D., Wirth, R., 2019. Specific multiphase assemblages of carbonatitic and Al-rich silicic Diamond-forming fluids/melts: TEM observation of microinclusions in cuboid diamonds from the Placers of Northeastern Siberian Craton. Miner. 9, 50.

Novella, D., Frost, D.J., 2014. The composition of hydrous partial melts of garnet peridotite at 6 GPa: implications for the origin of group II Kimberlites. J. Petrol. 55 (11), 2097–2124.

O'Reilly, S.Y., Griffin, W.L., 1988. Mantle metasomatism beneath western Victoria, Australia: I. Metasomatic processes in Cr-diopside lherzolites. Geochim. Cosmochim. Acta 52 (2), 433–447.

O'Reilly, S.Y., Griffin, W.L., 2013. Mantle metasomatism. Metasomatism and the Chemical Transformation of Rock. Springer, Berlin, Heidelberg, pp. 471–533.

Pasteris, J.D., 1984. Kimberlites: complex mantle melts. Annu. Rev. Earth Planet. Sci. 12 (1), 133–153.

Rock, N.M.S., 1991. Lamprophyres. Blackie, Glasgow 285 pp.

Rohrbach, A., Schmidt, M.W., 2011. Redox freezing and melting in the Earth's deep mantle resulting from carbon-iron redox coupling. Nature 472, 209–212.

Rosenthal, A., Foley, S.F., Pearson, D.G., Nowell, G.M., Tappe, S., 2009. Petrogenesis of strongly alkaline primitive volcanic rocks at the propagating tip of the western branch of the East African Rift. Earth Planetary Lett. 284 (1–2), 236–248.

Rudnick, R.L., McDonough, W.F., Chappell, B.W., 1993. Carbonatite metasomatism in the northern Tanzanian mantle: petrographic and geochemical characteristics. Earth Planet. Sci. Lett. 114, 463–475.

Sorbadere, F., Laurenz, V., Frost, D.J., Wenz, M., Rosenthal, A., McCammon, C., Rivard, C., 2018. The behaviour of ferric iron during partial melting of peridotite. Geochim. Cosmochim. Acta 239, 235–254.

Spandler, C., Yaxley, G., Green, D.H., Rosenthal, A., 2008. Phase relations and melting of anhydrous K-bearing eclogite from 1200 to 1600 C and 3 to 5 GPa. J. Petrol. 49, 771–795.

Spandler, C., Yaxley, G., Green, D.H., Scott, D., 2010. Experimental phase and melting relations of metapelite in the upper mantle: implications for the petrogenesis of intraplate magmas. Contrib. Mineral. Petrol. 160 (4), 569–589.

Stagno, V., Ojwang, D.O., McCammon, C.A., Frost, D.J., 2013. The oxidation state of the mantle and the extraction of carbon from Earth's interior. Nature 493, 84–88.

Stolz, A.J., Davies, G.R., 1988. Chemical and isotopic evidence from spinel lherzolite xenoliths for episodic metasomatism of the upper mantle beneath Southeast Australia. J. Petrol. 1, 303–330.

Sun, C., Dasgupta, R., 2019. Slab–mantle interaction, carbon transport, and kimberlite generation in the deep upper mantle. Earth Planet. Sci. Lett. 506, 38–52.

Sweeney, R.J., 1994. Carbonatite melt compositions in the Earth's mantle. Earth Planet. Sci. Lett. 128, 259–270.

Tappe, S., Foley, S.F., Jenner, G.A., Heaman, L.M., Kjarsgaard, B.A., Romer, R.L., Stracke, A., Joyce, N., Hoefs, J., 2006. Genesis of ultramafic lamprophyres and carbonatites at Aillik Bay, Labrador: a consequence of incipient lithospheric thinning beneath the North Atlantic craton. J. Petrol. 47, 1261–1315.

Tappert, R., Tappert, M.C., 2011. Diamonds in Nature: A Guide to Rough Diamonds. Springer Verlag, Heidelberg, Germany https://doi.org/10.1007/978-3-642-12572-0.

Taylor, W.R., Green, D.H., 1988. Measurement of reduced peridotite-COH solidus and implications for redox melting of the mantle. Nature 332, 349–352.

Tenner, T.J., Hirschmann, M.M., Humayun, M., 2012. The effect of H_2O on partial melting of garnet peridotite at 3.5 GPa. Geochem. Geophys. Geosyst. 13 (3).

Thibault, Y., Edgar, A.D., Lloyd, F.E., 1992. Experimental investigation of melts from a carbonated phlogopite lherzolite: implications for metasomatism in the continental lithospheric mantle. Am. Mineral. 77 (7–8), 784–794.

Tumiati, S., Fumagalli, P., Tiraboschi, C., Poli, S., 2013. An experimental study on COH-bearing peridotite up to 3.2 GPa and implications for crust-mantle recycling. J. Petrol. 54 (3), 453–479.

van Achterbergh, E., Griffin, W.L., Ryan, C.G., O'Reilly, S.Y., Pearson, N.J., Kivi, K., Doyle, B.J., 2004. Melt inclusions from the deep Slave lithosphere: implications for the origin and evolution of mantle-derived carbonatite and kimberlite. Lithos 76 (1–4), 461–474.

Wallace, M.E., Green, D.H., 1988. An experimental determination of primary carbonatite magma composition. Nature 335, 343–346.

Wallace, M.E., Green, D.H., 1991. The effect of bulk rock composition on the stability of amphibole in the upper mantle: implications for solidus positions and mantle metasomatism. Mineral. Petrol. 44, 1–19.

Walter, M.J., 1998. Melting of garnet peridotite and the origin of komatiite and depleted lithosphere. J. Petrol. 39 (1), 29–60.

Yaxley, G.M., Crawford, A.J., Green, D.H., 1991. Evidence for carbonatite metasomatism in spinel peridotite xenoliths from western Victoria, Australia. Earth Planet. Sci. Lett. 107, 305–317.

Zedgenizov, D.A., Rege, S., Griffin, W.L., Kagi, H., Shatsky, V.S., 2007. Composition of trapped fluids in cuboid fibrous diamonds from the Udachnaya kimberlite: LAM-ICPMS analysis. Chem. Geol. 240 (1–2), 151–162.